DEVELOPMENT OF INNOVATIVE SOFCS BY COLLOIDAL PROCESSES AND CO-SINTERING TO BE USED BY BIOFUELS

Doctoral School in Materials, Mechatronics and System Engineering

Cycle XXXV
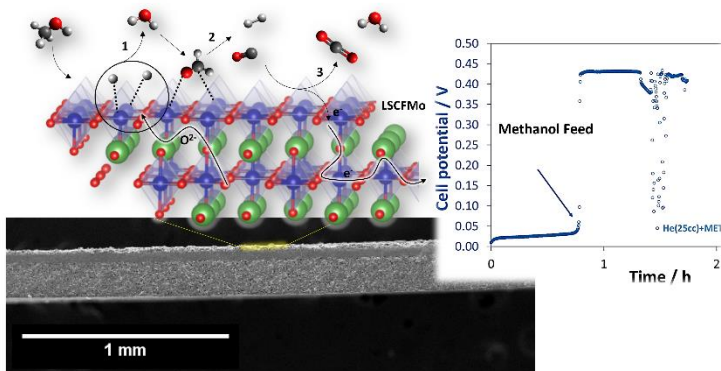
Kimia Yousefi Javan

October 2023

Development of Innovative SOFCs by Colloidal Processes and Co-Sintering to be Used by Biofuels

Kimia Yousefi Javan

Kimia.yousefijavan@unitn.it

Approved by

PhD Committee

Prof. Vincenzo Maria Sglavo

Department of Industrial Engineering

University of Trento

Prof. Elisabetta Di Bartolomeo
Department of Chemical Science and Technologies
University of Rome Tor Vergata

Prof. Rodrigo Moreno
Institute of Ceramics and Glass CSIC

I would like to pass on my ...

Thanks to my family who has supported me over the years, especially my mother and father, who have always been there for me without expecting anything in return, giving me the power and strength to conquer hurdles!

Thanks to my professor, who accompanied me through this process with generosity and patience, allowing me to grow and bloom in science and new experiences every day!

Thanks to my friends for providing me with enjoyable and wonderful memories during these years!

Thanks to the Minister of Education in Italy, my university, admissions committee members, and all the nice administrative personnel who made this opportunity possible for me to seize and explore!

Abstract

Climate change and environmental degradation, in addition to the challenges of limited fossil fuel resources, have driven governments to pursue creative renewable energy sources. Natural gas and biofuels are limitless energy sources produced from both fossil fuels and biomass that is renewable. SOFCs (Solid Oxide Fuel Cells) are a type of renewable energy system that can convert biofuels into power and heat whenever needed. They often operate at high temperatures (> 850 °C), which allows for fuel flexibility; nevertheless, such high temperatures are associated by rapid material deterioration and performance loss, usually before 40,000 hours of operation. As a result, many recent studies and activities have concentrated on lowering the operating temperature of SOFCs. Lowering the temperature causes decreased ionic conductivity, decreased catalytic activity, and increased carbon deposition on the anode side catalysts.

This project aimed at developing an innovative cathode-supported SOFC to be fed by biofuels and operating at low-intermediate temperatures. Colloidal processes and co-sintering were selected to fabricate the final SOFC owing to their flexibility in optimizing the final desired properties and saving more manufacturing costs.

The first chapter of this thesis provides an introduction to the essential concepts as well as professional specifics and previous work. The cell design and component materials are defined, as are additional requirements for lowering the operating temperature in SOFCs. Commercialization challenges and recommended solutions are also discussed, which involve the development of both new anode materials and production procedures. The project's goal is detailed at the end of Chapter 1, along with the reasons why various approaches were chosen. Molybdenum was chosen as a suitable anodic material to be doped into LSCF, and tape casting was developed further to create the cathode. The cathode support layer should have a consistent thickness, balanced flexibility and mechanical strength, and better shrinkage qualities. The plasticizer is a high molecular weight

polyethylene glycol (PEG 4000), which improves these characteristics.

Chapter 2 covers the steps involved in creating the button SOFC, starting with powder synthesis and ending with cathode tape casting. SOFC performance and anode catalytic activity are investigated to assess SOFC durability while fed by biogas.

In Chapter 3, the findings are presented and explored in various contexts. Meanwhile, the anode material performance and cathode design and structure receive the greatest attention. Molybdenum was doped into LSCF via auto-combustion, yielding a fine and porous powder form. X-ray diffraction patterns demonstrated that increasing the Mo dopant increases anodic stability. In parallel, flat and crack-free green cathodes with 47% solid loading can be obtained by adjusting the PEG 4000 to binder quantity ratio at 1.00 wt% and drying the tapes at 70% relative humidity. The tapes had an excellent mechanical strength to flexibility ratio, which allowed them to be readily handled and rolled. The tapes benefited from a strong balance of flexibility and mechanical strength, allowing them to be easily handled and rolled while also exhibiting very low residual stresses during subsequent lamination and co-sintering procedures. The final manufactured SOFC revealed a porous anode structure and a less porous cathode layer using electron microscopy. Whereas the electrolyte was dense enough to ensure gas tightness. There was no delamination throughout the cell. The cells were then electrochemically measured, and the reactivity of LSCFMo to various fuels and temperatures was investigated. LSCFMo performed best when fed by methanol at 700 °C, leaving no carbon traces after operation. The very low ohmic resistance of the electrodes indicates a very good design and manufacture technique.

A conclusion is presented in the final section of this thesis to highlight the most significant achievements of this research.

Index

List of Figures

List of Tables

CHAPTER 1

Introduction

1.1 Renewable Energy Systems

Concerning population and economic growth, in parallel with advancing technology, the global demand for energy production is increasing each year by 1.3%. Although fossil fuels are the primary source that fulfils up to 85% of the world energy demand now [1], the amount of CO_2 emission by their consumption and the subsequent climate change issues besides the fact it is a finite source that is going to be depleted within 50 years at current use level [2], has prompted the governments to seek for alternative renewable energy sources.

Renewable energies (RE) are infinite primary energy resources on the earth such as solar radiation, wind, water energy, geothermal heat or biomass that can be captured and converted into final heat and electricity. The systems that run this conversion from mentioned energy carriers to consumable energies are called "renewable energy systems (RES)" [3]. The main RES are wind turbines, photovoltaic solar panels, hydropower plants and fuel cells. Although the annual energy production by RES can be much greater than the global energy demands each year, RE sources availability fluctuates. For example, when it is cloudy, solar panels cannot produce energy efficiently while on sunny days, there is no wind. Additionally, oversizing RES to supply the energy demand is costly. The solution is to provide a large-scale storage system or to develop hybrid RES which is still under development in sense of market, policy, and technical approaches. Thus, the priority is on extracting, transporting and converting fossil fuels [4], [5] that not only can be consumed by RES but also can be substituted by similar RE sources in future.

Natural gas and biofuels are such kinds of energy sources that can be derived from both fossil fuels and renewable biomass. They can be converted into electricity through hydrogen, as an energy carrier, and with the help of fuel cells operating as RES (Figure 1.1).
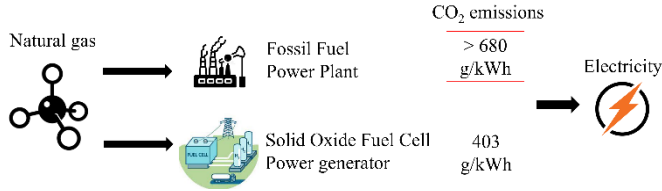
Figure 1.1 Carbon emissions in g/kWh from a fossil fuel and an RES plant

1.2 Advanced Systems for Energy Production

Advanced RES are needed to guarantee energy sustainability in future by producing energy more efficiently and significant savings. Thus, such systems are required to work independently by RE sources and be available where and when needed [6].

Hydrogen is a synthetic fuel that can be stored and converted to electricity in place and at the time there is a need. Hydrogen is not an energy source itself but can carry energy from one form into another [7]. For example, in wind and solar RES, the excess produced electricity can be used to electrolyze the water to obtain hydrogen [8]. Biomass is another type of RE, made of wood and agricultural residues, food crops and municipal-industrial organic wastes. It can be converted into biofuels and hydrogen by pyrolysis or gasification conversion processes [9], and then the hydrogen can be fed into fuel cells to generate electricity. Conversion means when the primary energy is processed and turns into other forms of energy [10]. However, it is accompanied by losses in efficiency which leads to a low power yield at the end [11]. Advanced RES are made to reduce the conversion efficiency loss as much as possible like solid oxide fuel cells (SOFC).

SOFC is a developed version of fuel cells that can be fed directly by biofuels and light hydrocarbons, with no need for pretreatment of fuels. Additionally, because the chemical reactions in SOFCs are not limited to the same as in combustion engines and Carnot cycles, SOFCs are accompanied by the highest energy conversion efficiency of up to 80% [12].

1.3 Low/Intermediate-Temperature Solid Oxide Fuel Cell (LT/IT-SOFC)

It was first in the late 1930s that a Swiss scientist, Emil Baur and his colleague Hans Preis started to experiment with the first fuel cell (Figure 1.2) with a solid electrolyte made of ceramics: 15 wt% Yttria and 85 wt% Zirconia (Nernst Mass), in National Energy Technology laboratory [13].

Figure 1.2 1.5-meter SOFC bundle, Westinghouse

SOFC is a fuel cell that converts chemical energy directly into electricity and heat, out of conversion of biofuels and without any combustion. As shown in Figure 1.3, SOFC is made of main components such as anode, electrolyte, and cathode layers, contact materials, interconnects, and sealants. On the anode side, fuels and hydrogen are oxidized using catalysts to produce electrons. Electrons run through an external circuit towards the cathode. In the cathode, oxygen reacts with entering electrons and is reduced to produce oxygen ions which then pass through a dense ion-conductive electrolyte towards the anode. At the anode/electrolyte interface, ions react with hydrogen to produce water and release electrons. Assuming that the electrodes are constantly supplied with fuel and oxygen, this cycle is repeated and the electricity is generated continuously [14].
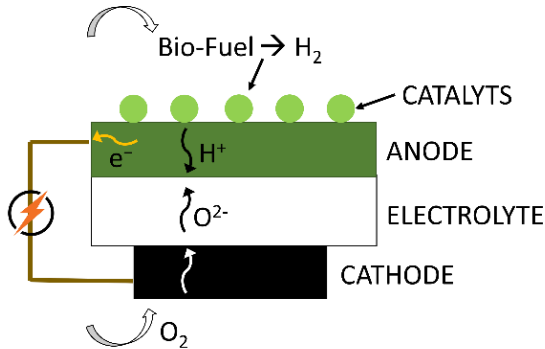
Figure 1.3 Schematic of an SOFC

SOFCs usually work at high temperatures and due to this, there are more advantages to using them than other types of fuel cells. Fuel flexibility, faster electrode electrocatalytic activity and the possibility to be integrated with other power generation systems (due to the significant amount of waste heat) are the most important advantages of high-temperature SOFCs (HT-SOFC). Since SOFCs are one of the most important technologies for energy conversion with the most development focus on stationary applications, one critical factor in their commercialization is the long-term durability and the capability to store or reverse the produced electrical energy [15]. However, high temperatures can lead to deterioration of both SOFC and balance of plant (BOP) materials which increases the costs of maintenance. Long-term start-up and performance degradation, usually before reaching a lifetime of 40,000 h, are other factors which strongly call into question the viability of commercializing biogas SOFC that can limit the life of the system at high temperatures [16].

To address such issue, the research is prompted towards the development of low/intermediate temperature SOFCs (LT/IT-SOFC) operating in the range 500–600°C for LT and 600–800°C for IT, which offers many advantages such as faster start-up and shutdown, slower corrosion of interconnect or sealant materials, improved cell durability and, therefore, cost savings [17]. Owing to these advantages, the goal of many SOFC-manufacturing companies is to reach LT/IT-SOFCs into the mass market so that they not only can be applied to a wider

variety of industries but also can be used for portable and more interesting than that, for transportation section of industry [18]. The downside of operating at low temperatures, though, is the lower ionic conductivity and higher electrical polarization [19] which both limit the fed flexibility and decrease the power output at low temperatures.

To pass these limitations, LT/IT-SOFC must be re-designed and optimized in terms of main trends:

- fuel type,
- cell design,
- component materials,
- and the specific operating temperature,

thus the highest possible power output can be obtained [20].

1.4 Fuel Type

There are different types of fuels for SOFCs, from the simplest which is hydrogen to complex hydrocarbons like gasoline, jet fuels and biogas. SOFCs can be fed by heavy fuels as well as light ones and reformed into hydrogen and CO_2/CO. Biogas plays an important role in the global energy transition from fossil fuel-based plants to renewable power generation systems. It can be produced from renewable biomass sources locally, does not face the challenges of storage and does not contribute to the annual growth cycle of carbon dioxide emissions. Thus, it emerges as the most promising alternative to fossil fuels for a sustainable energy system in future. It generally contains 30-70% methane and 30-50% carbon dioxide, with little amount of hydrogen [21].

Reforming Reactions

There are two forms of reforming: external and internal. Heavy fuels are reformed externally into hydrogen and CO_2 usually before entering the SOFC. In internal reforming, light fuels can be reformed inside the SOFC system in steam, partial oxidation or dry mode, while

electrochemical reactions take place simultaneously on the anode side [22]. HT-SOFCs can perform internal reforming of even heavy fuels, due to the high catalytic activity of catalysts at high temperatures, whereas LT/IT-SOFCs can be fed only by light hydrocarbons. Although biogas is considered a heavy fuel, it can be fed directly into LT/IT-SOFCs and be dry reformed internally, with the help of the high amount of carbon dioxide that it contains. However, the possibility of coking and carbon deposition must be considered in this situation due to the high CO_2 amount [21]. In the end, the power density obtained from a biogas-fed SOFC is lower than the pure hydrogen-fed SOFC due to both efficiency loss in biogas reforming reactions, and the carbon formation. Thus, it is important to increase the efficiency of biogas reforming by engineering anode materials and designing suitable catalysts [23].

Because methane conversion in biogas reforming is much slower than CO and hydrogen oxidation, the dry reforming of methane is considered, and its reforming reaction is given by

$$CO_2 + CH_4 \rightleftharpoons 2H_2 + 2CO \qquad \Delta H^{\circ}_{298} = 247.3 \, kJ/mol \qquad (1.1)$$

$$H_2 + CO_2 \rightleftharpoons CO + H_2O \qquad \Delta H^{\circ}_{298} = 41.1 \, kJ/mol \qquad (1.2)$$
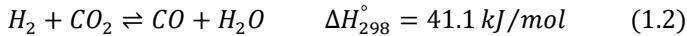
which are high endothermic reactions. Thus, for a complete reforming reaction, either the operating temperature should be high enough (800-1000 °C) or at low-intermediate temperatures (< 800 °C), CO_2 must be supplied by another additional source [24].

1.5   Cell Design

As mentioned before, lowering the operating temperature can affect the ionic conductivity, polarization, and chemical compatibility of the materials in SOFC components. Accordingly, the structure of a SOFC should be designed to compensate for the negative effects of low temperature and to obtain the highest possible open-circuit voltage (OCV) out of the cell. The final actual OCV of a SOFC is given by

$$E_{cell} = E_{Nernst} - \eta_{ohm} - \eta_{act} - \eta_{conc} - \eta_{f.cr} - \eta_{in.curr} \qquad (1.3)$$

where E_{nernst} is the ideal cell OCV, η_{ohm} the ohmic polarization, η_{act} the activation polarization, η_{conc} the concentration polarization, $\eta_{f.cr}$ the loss due to fuel diffusion into the electrolyte and $\eta_{in.curr}$ the loss due to short-circuit of the electrolyte [25]. HT-SOFCs can be supported by their thick dense electrolyte layer. Due to the greater thickness of the electrolyte, larger ohmic polarization resulted, which can be reduced at high temperatures [26]. However, dealing with this issue at low temperatures is possible either by decreasing the electrolyte thickness or by increasing its ionic conductivity [17]. As the electrolyte gets thinner, more attention must be paid to its tightness and gas impermeability, besides the fact that during sintering, the electrolyte layer can penetrate electrodes.

Lowering the temperature can also affect the oxygen reduction reaction (ORR) on the cathode side and slows it down. This causes a high concentration polarization due to the accumulation of electrons inside the cathode and high current density at the surface of the electrode. To solve this issue at lower temperatures, the cathode composition and microstructure should be well-designed and should benefit from enough porosity to facilitate the rapid transfer of O_2 to active sites [19].

Thinner anode layers in a cathode-supported SOFC are preferred at lower temperatures, thus preventing carbon build-up from working with biogas and reducing the polarization resistance. Figure 1.4 illustrates the schematic of a cathode-supported LT-SOFC. The porosity of the anode should meet a range within the limitations not too large to create high $\eta_{f.cr}$ and not too small to hamper the effective electrocatalytic activity of catalysts [27].

Button-cell design is a recent novel approach in fabricating SOFCs, in a thin, small circular shape with a diameter of 1–3 cm. Button-cell design is proposed to improve materials selection, achieve better-controlled microstructure and processing, and easier evaluation, characterization and performance configuration of final samples [28].
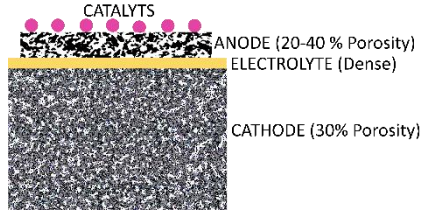
Figure 1.4 Schematic of a cathode-supported LT-SOFC

To fulfil the microstructure and design requirements, component materials should be selected with high precision and based on their chemical and thermal compatibility with other materials in the neighbour components.

1.6   Component Materials

The materials selection for SOFC should be made based on the functionality of the component and the operating temperature of the SOFC. The main factors to be considered during the material engineering of electrodes and the electrolyte in LT/IT-SOFCs are thermal expansion coefficient (TEC), phase and composition stability, electronic and ionic conductivity, electrocatalytic activity and final desired microstructure.

1.6.1   Cathode

The electrochemical (Kröger-Vink) reaction at the cathode side of a biogas-fed SOFC is given by [29]

$$\frac{(3n+1)}{2} O_2 + (6n+2)e^- + (3n+1)V_{\ddot{O}} \rightarrow (3n+1)O_O^x ; \quad (1.4)$$
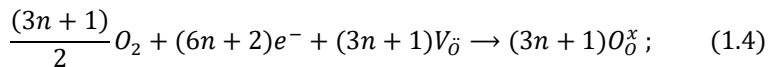
therefore, a good cathode should satisfy the following requirements [30]:

- High catalytic activity towards ORR
- High mixed ionic and electronic conductivity (MIEC)

- Adequate porosity
- Matching TEC with electrolyte and other components
- In the case of cathode-supported cells, a high mechanical strength

Perovskites are one kind of MIEC materials that are proposed as the best materials for cathodes with the general formula ABO_3 containing an alkaline/rare-earth metal cation in A-site and a transition metal (M) cation with smaller radii in B-site. Perovskites are generally divided into four main groups: single, double, layered and exsolved. Thanks to high flexibility in substituting A and B cations, the final desired feature of a material can be achieved [31].

$La_{1-x}Sr_xFeO_{3-\delta}$ (LSF) and $La_{1-x}Sr_xCoO_{3-\delta}$ (LSC) are the most common conventional cathode materials in SOFCs, regardless of the operating temperature in addition to $La_{1-x}Sr_xCo_yFe_{1-y}O_{3-\delta}$ (LSCF), $La_{1-x}Sr_xMn_{1-y}Co_yO_{3-\delta}$ (LSCM) and $Ba_{1-x}Sr_xFe_{1-y}Co_yO_{3-\delta}$ (BSCF) with higher surface exchange and diffusion rate [32]. Although cobalt-containing oxides (e.g. LSCF) possess higher electroconductivity ($\approx$ 1000 S cm^{-1} at 800 °C), they show large TEC as well with respect to non-cobaltite perovskites (e.g. LSF) [33]. Insufficient chemical compatibility, high cost, easy evaporation and weak chemical stability have been considered recently as discouraging factors in using cobalt-containing cathodes [34]. Another disadvantage of using cobaltite is that it can easily react with Cr-containing contact layers and get chromium poisoned.

In this regard, and considering the high TEC of LSCF, the residual stresses during cathode-electrolyte lamination and further co-sintering are reduced using LSF.

1.6.2   Electrolyte

The requirements which make a good electrolyte out of a material are as follows:

- Full density
- Pure ionic conductivity

- Engineered vacancy in lattice structure.

Since the vacancy mechanism is activated by thermal energy, the electrolyte is the main part of a cell that determines the final operating temperature. To prevent the formation of any local hot spot inside the electrolyte, it must be free of any hole or porosity. These two together indicate the importance of the choice of material and fabrication method for the electrolyte [35].

Yttria-stabilized zirconia ($ZrO_2.Y_2O_3$: YSZ) is the conventional electrolyte material in SOFCs but with vacancy activation only at high temperatures like in HT-SOFCs. Zr in YSZ also reacts with Sr in the LSF cathode and forms an insulated $ZrSrO_3$ phase which degrades the cell performance [36]. To have an efficient electrolyte for LT/IT-SOFCs, either the thickness of YSZ should be decreased or another promising material with a higher ionic conductivity must be selected, like gadolinium-doped ceria ($Gd_xCe_{1-x}O_{2-(x/2)}$: GDC) [37]. GDC is preferred over YSZ due to its higher ionic conductivity below 800°C, which becomes more evident even at lower temperatures and because it does not react with Sr in the cathode material [38].

1.6.3 Anode

Working with biogas-fed LT-SOFC, an anode is considered the most important component. Reforming of hydrocarbons, their electrochemical oxidation, conducting the electrons and at the same time, the oxygen ions, should be carried out simultaneously by the anode at low temperatures where catalytic and electrochemical activities are significantly low. Thus, the anode material selection and its engineering demand good reliability.

Ni-YSZ represents the traditional cermet anode material, which is still widely used in industry. It is cost-effective, easy to fabricate, has excellent electronic conduction due to Ni particles and an excellent ionic conductivity owing to YSZ [39]. Additionally, Ni catalytic activity at high temperatures (850–1000 °C) is sufficient enough that there is no need for precious metals [40]. Despite all these merits, it cannot guarantee the sustainability of LT-SOFCs due to serious

drawbacks. Electrochemical (Kröger-Vink) reactions at the anode side are given by [29], [41]

$$C_nH_{2n+2} + (3n+1)O_O^x$$
$$\rightarrow (3n+1)V_{\ddot{O}} + nCO_2 + (n+1)H_2O + (6n+2)e^- \quad (1.5)$$

$$O_O^x + H_2 \rightarrow V_{\ddot{O}} + 2e^- + H_2O \qquad (1.6)$$

$$O_O^x + CO \rightarrow V_{\ddot{O}} + 2e^- + CO_2 \qquad (1.7)$$
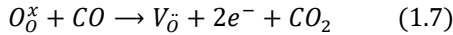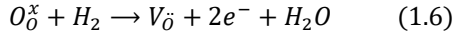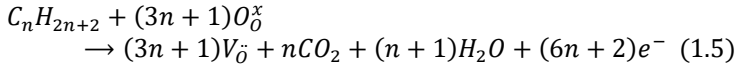
Methane oxidation and oxygen ion pathway towards the anode surface is shown in Figure 1.5.
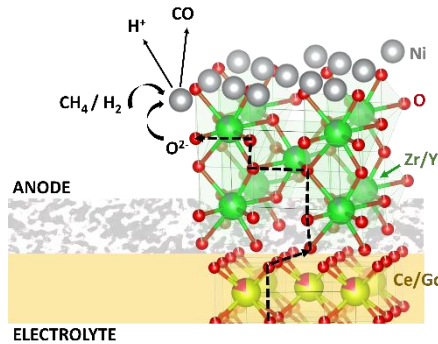
Figure 1.5 Methane Oxidation at the Ni-YSZ surface

Thus, a good anode electrode should fulfil the following requirements [42]:

- matching TEC with the electrolyte and other components,
- high electroconductivity,
- capability to dodge the coke,
- large porosity (20–40%) to transfer the fuel easily,
- large triple phase boundaries (TPB) to increase electrochemical activity,
- high catalytic activity at low temperatures and,
- the high ionic conductivity,

from which, some are lacking by Ni-YSZ cermet. Accordingly, there is a wealth of literature on investigating Ni-YSZ drawbacks and proposing possible solutions.

Drawbacks

There are major issues caused by Ni particles that have prompted the academic and industry research world to seek new alternative materials as the anode for SOFCs. Ni-YSZ cermet can be used to convert hydrocarbons completely, only in wet mode, where the steam is supplied for internal reforming [43]. Low tolerance to coking and carbon deposition at low temperatures (<800 °C), vulnerability to sulphur poisoning, Ni coarsening and poor redox and volume stability during redox cycling in the case of biogas-fed SOFCs, are other limitations of Ni-YSZ anodes [44].

i.   Carbon Deposition

Carbon deposition is the main issue with the anode, while SOFC is fed by hydrocarbons. During hydrocarbon reforming reactions, whether at high or low temperatures, solid carbon is formed due to fast C–C bond cracks, carbon diffusions and aromatic reactions. Based on the operating temperature and the catalyst type, the deposition mechanism is different. In the case of Ni catalyst, due to the high catalytic activity of Ni, the solid carbon is dissociated from hydrocarbons, deposits on top of Ni surface and then diffuses into grains and precipitates at the end. This is fatal and compromises the cell integrity, which is accompanied by rapid performance degradation [45]. At high temperatures, methane thermal cracking can form solid carbon in graphitic shape which deposits on and encapsulates catalysts, leading to their deactivation. At low temperatures, though, solid carbon is formed following the Boudouard reaction, as

$$2CO \leftrightarrow CO_2 + C \qquad \Delta H^{\circ}_{298} = -171 \ kJ/mol \qquad (1.8)$$
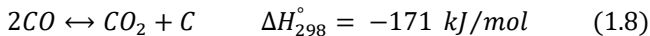
or water-gas reverse-shift reaction, which leads to CO reduction, as

$$H_2 + CO \leftrightarrow H_2O + C \qquad \Delta H^{\circ}_{298} = -131 \ kJ/mol \qquad (1.9)$$
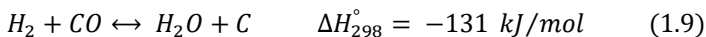
in an amorphous and whisker-deposited form. Due to the growth of carbon chains, it diffuses into catalyst grains, deactivates them and increases the internal stresses which cause the cell rupture and delamination at the anode-electrolyte interface [46]. The carbon deposition mechanism is shown in Figure 1.6. By designing an anode structure with suitable catalytic activity and good oxygen ionic conductivity, carbon deposition can be suppressed.
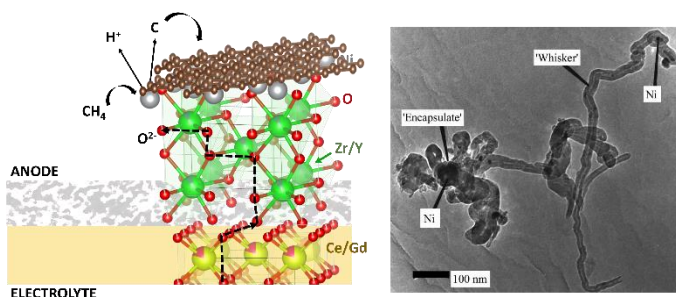
Figure 1.6 Carbon deposition mechanism on Ni catalysts (left) and electron micrograph of a whisker deposited carbon on Ni catalyst (right) [47]

ii.   Low Redox Stability

Taking the redox stability of anodic structure into account is important in the choice of anode material. The low redox stability of conventional Ni-YSZ cermet has been well investigated. Both electrical conductivity and phase volume of Ni-YSZ are affected by the reduction temperature and redox cycle. Higher electroconductivity is achieved by increasing the reduction temperature while low electroconductivity is achieved by being reduced at low temperature and is not improved by further heat treatments. This means Ni is reduced simultaneously with being sintered, thus an irreversible change in grain size is exerted. Additionally, Ni phase volume is expanded upon re-oxidation due to NiO formation which is followed by simultaneous reduction and sintering. This volume expansion reduces available TPB and if exceeds the porosity capacity, not only causes fractures in the YSZ substrate but also exerts stresses in the electrolyte and finally ruptures the cell [39]. Despite many efforts that

have been made to solve this issue [40], Ni-YSZ anodes do not satisfy the stability needed in long-term applications.

Perovskites are proposed as the best alternative for SOFC anodes. Due to their high oxygen vacancy, O^{2-} conduction increases which ends with faster fuel oxidation at the anode. They can also extend the TPB from the anode/electrolyte interface up to the surface of the anode; this means more active sites and greater electrochemical activity. Nevertheless, still, electronic conductivity, catalytic activity and phase stability of perovskites need to be improved to yield a performance comparable with conventional anodes [48].

1.7 Innovative Materials

To manage the anode issues, numerous studies have suggested innovative alternatives to Ni-YSZ, which for their development, the ceramics are indispensable, including nanostructured composites, multi-metal alloys, single and polycrystals, exsolved perovskites and doped-perovskites. Among them, fabricating advanced anodes using perovskites is the most reliable and cost-effective approach. Doping elements of high coke resistance and phase stability into the A/B-site of perovskites can tune the hole and vacancy formation and subsequently, optimize their electronic-ionic conductivity [49].

Coke-Resistant and Redox-Stable Doped-LSCF

To increase the coke resistance of perovskites, the structure should be supplied with adequate oxygen vacancies or high surface exchange capability [50]. Doping cations into B-site, with more unoccupied 3d orbitals exerts higher catalytic activity, which favours faster oxidation of the deposited carbon into CO or CO_2, as well as more efficient fuel oxidation. Another characteristic in B-site cations that can help mitigate carbon deposition is possessing higher oxidation states. Such cations are capable of loading and unloading oxygen ions and fast switching between their oxidation states, thus helping with faster oxidation of the deposited carbon and cleaning TPBs off the diffused

carbon. Some other cations like Cu and precious metals are inert in carbon absorption [51]. To increase the perovskite's redox stability, B^+ reduction must be prohibited under reducing conditions and its energy either must be increased by altering temperature or pH or must be covered by a greater band gap energy belonging to a sacrificing doped-cation.

$La_{0.75}Sr_{0.25}Cr_{0.5}Mn_{0.5}O_{3-\delta}$ (LSCrM) was the first perovskite anode, proposed by Tao et al. [43] in 2003, to address Ni-YSZ issues. Mn doping into chromate-based perovskites can increase their phase redox stability and Montinaro et al. [52] also realized LSCrM laminates with the usage for anode-supported SOFCs. But this material must deal with electroconductivity issues. Titanate-based perovskites are also another promising anode material with the backbone formula $SrTiO_3$. However, they are accompanied by issues of electrochemical and catalytical activity [53]. A recent work by Bugra et al. [54] made an increased surface catalytic activity of $SrTiO_3$ which is sufficient for hydrocarbon conversion, by doping it with La^{3+} and enrichment of the surface by Sr segregation.

Lanthanum ferrites are another interesting family of perovskites with superior advantages over other families and with the general formula $LaFeO_3$ (LFO). LSCF has been one of the most widely studied cathode materials since the beginning of the '90s till now [55]–[57], due to its optimum tolerance factor and high oxygen vacancies for both A and B site doped structures, combined with high electroconductivity. Doping Sr at the A-site can act as an acceptor and Co at B-site binds stronger with Fe relative to oxygen. These two bring about an increase in the oxygen permeability of the structure which is followed by good catalytic activity towards oxygen reduction reaction at the cathode side and an increase in TPB [33]. This is while not much attention has been given to possible anode applications.

Few studies have shown the good possibility of applying LSCF as an anode while it can decompose to $(La_{0.38}Sr_{0.62})_2FeO4$ and La_2CoO_4 Ruddlesden-Popper (R.P.) oxides, and CoFe alloy nanoparticles under low oxygen partial pressures, accompanied by good catalytic activity of CoFe alloys towards hydrocarbons reforming reactions [58]. Although R.P. LSCF oxide has shown higher oxygen ion conductivity

than normal perovskite, the electronic conductivity is still relatively small due to the interrupted transition metal-oxygen-transition metal chains [59]. Doped-LSCF can be functionalized with surface exsolution as well. Dopants are exsolved towards the surface and then socket on top of parent perovskite and form a nanometric single/multi-metallic alloy on top, usually with high catalytic activity towards hydrocarbons reforming and less coke-absorbance. Lo Faro et al. [60] have worked on Ni-doped LSCF and investigated its efficiency as an anode being fed with different fuels. Such doped-lanthanum ferrites show very poor catalytic activity towards the direct oxidation of methane. Instead, another mechanism called the "shuttle mechanism" is followed which works with fuels other than biogas and methane. This mechanism starts with the dehydrogenation of fuels and continues with the subsequent oxidation of hydrogen and carbon monoxide residues [60]. Whether the perovskite carries out a "shuttle mechanism" or direct oxidation of methane, their structural stability and low electroconductivity under reducing conditions can still hinder their practical applications in industry.

1.8   Molybdenum Doping

Doping elements of higher valence such as Cr, Mo,W, V, Nb, Ti, and Zr into B-site of a perovskite structure specifically the ferrites can bring great advantages for both anode and cathode applications. This will increase their long-term stability as electrode materials under both oxidizing and reducing conditions [61], as well as tunning their oxygen vacancies. Molybdenum is an element with a higher proportion of unoccupied 3d-orbitals, possessing both mixed and higher valence states. Mo-based perovskites have been proved in different studies to exert amazing properties for the application of electrode materials in fuel cells, depending on the parent perovskite and the dopant amount.

B-site doping in LSCF with molybdenum as a high valence acceptor dopant can improve redox stability to a great extent. Previous studies proved that by doping Mo into $Ba_{0.5}Sr_{0.5}Co_{1-x}Fe_xO_{3-d}$ [62], [63],

and $La_{0.5}Sr_{0.5}FeO_{3-\delta}$ [64] the reduction stability increased remarkably. At low partial oxygen pressure, molybdenum can moderate further reduction of Fe^{3+}/Fe^{2+} into the metallic phase. This is due to the overlap between the redox band of mixed-valent Mo^{5+}/Mo^{6+} and Fe^{3+}/Fe^{2+} couples in most Mo-doped ferrites [65], which is also proved by XPS investigations [66]. As a result, no new metallic alloy or R.P. oxides will form under reducing conditions, and the perovskite retains its chemical stability. However, under oxidizing conditions, the mechanism that Mo increases the phase stability is different. Y. Liu et al. [67] doped Mo into LSCF structures as cathode material. XPS results showed interestingly that the ratio of Sr segregated on the surface to the Sr in the lattice was decreasing by increasing the Mo dopant. In other words, Mo could suppress the Sr dissolution. This could save the perovskite structure from degradation under oxidizing conditions which could bring about a better electrocatalytic activity towards oxygen reduction reaction. In another work, Neacsa D. et al. [68] showed that doping higher valance elements like Nb^{5+} with higher ionic radius into the B-site of LSCF can afford more accommodation for Sr^{2+} at A-site. As a result, Sr activation might be suppressed, and the phase stability increases during sintering.

Electrocatalytic activity and performance of perovskites is mainly dependent on concentration of their oxygen vacancies. Many studies have proved that Mo doping into ferrite perovskites enhances the oxygen vacancy formation in the structure [66][69][70][71]. Figure 1.7 shows the results from X-ray photoelectron spectroscopy (XPS) which was carried out on the surface of $Sr_2FeMo_{0.65}Ni_{0.35}O_{6-\delta}$ and $La_{0.6}Sr_{0.4}Fe_{1-x}Mo_xO_{3-d}$.

These results have confirmed the co-existence of mixed-valence state couples Mo^{5+}/Mo^{6+} and $Fe^{2+}/Fe^{3+}/Fe^{4+}$ on the surface of Mo-doped ferrite perovskites. By increasing Mo dopant, the amount of Fe^{3+} will increase to compensate for the electroneutrality. Fe^{4+} at the center of octahedral takes the electron holes from the neighbor lattice oxygen and is reduced to Fe^{3+}, while the lattice oxygen is released. As a result, more oxygen vacancies can be formed as [72][70]

$$2Fe_{Fe}^{\bullet} + O_O^{\times} \longrightarrow 2Fe_{Fe}^{\times} + V_O^{\bullet\bullet} + \frac{1}{2}O_2 \qquad (1.10)$$
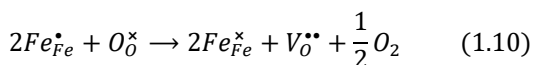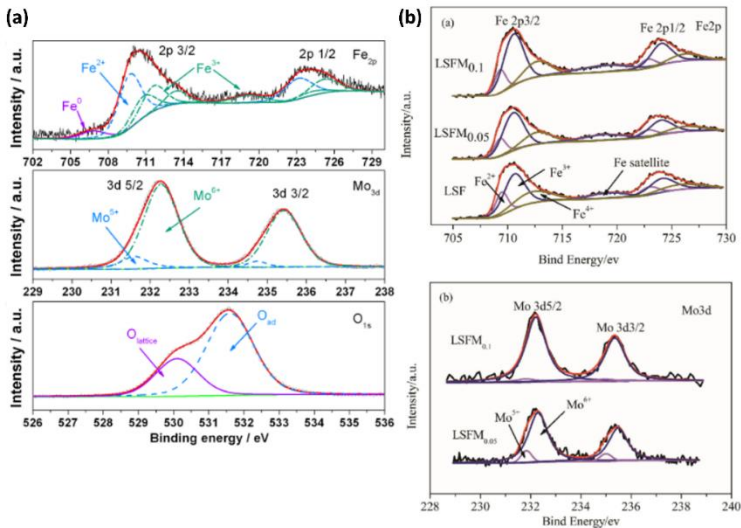
Figure 1.7 XPS spectra of a) SrFeMoNi [66] and b) LaSrFeMo [69] perovskites, Mo 3d and Fe 2p

When the amount of Mo dopant increases or the perovskite works under reducing conditions (when Fe^{4+}/Fe^{3+} reduction is relieved to some extent by the presence of the mixed valence Mo^{6+}/Mo^{5+}), Mo^{6+} reduces partially to Mo^{5+} to keep up with the electroneutrality in the structure, which means even more oxygen vacancy formation, as [73]

$$2Mo_{Mo}^{x} + O_{O}^{x} \longrightarrow 2Mo_{Mo}' + V_{O}^{\bullet\bullet} + \frac{1}{2}O_2 \qquad (1.11)$$
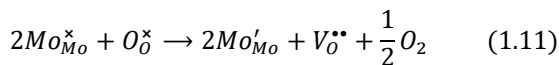
More oxygen vacancies benefit more active sites generation and thus more electrocatalytic activities. As a result, TPBs are enlarged which leads to a better electrocatalytic activity towards hydrocarbon reforming reactions. As proved by XPS studies, the peaks of binding energy for Mo 3d is observed at around 230 eV, while for Fe 2p, the peaks are observed at around 700 eV. Thus, oxygen transferring which means the capability to load/unload the oxygen ions is more facilitated through Mo cations, thanks to its higher proportion of unoccupied 3d-orbitals and mixed valence states. As a result, the electrocatalytic activity increases as Mo dopant is increasing.

These studies have also confirmed that the ratio of adsorbed oxygen (O_{ad}) to the lattice oxygen in Mo-based perovskites is increasing by an increase in Mo dopant amount. Since at high temperatures, O_{ad} can be easily desorbed, the conclusion is that Mo could efficiently increase the oxygen vacancies [72][66]. In addition to this, Zhang et al. [72] found that doping Mo into the perovskite structure $Pr_{0.4}Sr_{0.6}Co_{0.2}Fe_{0.8}O_{3-\delta}$ can decrease the surface-phase amount, which is in favor of the catalytic reactions. Wang et al. [69] doped Mo into $La_{0.6}Sr_{0.4}FeO_{3-\delta}$ and achieved higher electrocatalytic activity at the surface towards CO_2 electrolysis, due to Fe-O-Mo pairs which can store higher oxygen ion species. Liu et al. [67] could also achieve better electrocatalytic activity towards oxygen reduction reaction by doping Mo into LSCF cathodes.

Furthermore, Mo-doped perovskites have proved to direct good electroconductivity due to presenting mixed valence couples and to adopt different arrangements of oxygen polyhedral from tetragonal to six-fold coordination, which makes it compatible with accepting a wide range of oxygen stoichiometries [74]. Hou Y. et al. [75] showed that the higher reduction stability can also bring about an increase in electroconductivity of Mo-doped $La_{0.6}Sr_{0.4}Fe_{0.9}Ni_{0.1}O_{3-\delta}$, at a wide temperature range (500-850 °C). Although higher-order R.P. oxides exhibit enhanced electroconductivity [76], first-order newly generated R.P. oxides after LSCF reduction, such as $(La_{0.38}Sr_{0.62})_2FeO_4$ and La_2CoO_4, have been shown to have good but lower electroconductivity than the parent perovskite. Park et al. [59] and Chung et al. [77] attributed the explanation to fewer B-O-B bridges in first-order R.P. oxides, which often serve as the electron channel. Higher reduction stability can protect the bond bridge $Fe^{3+}–O^{2-}–Fe^{4+}$ in the structure which prevents further increase in the activation energy of electron transfer. Thus, higher conductivity can be expected relative to pure perovskite [75]. On the other hand, some studies have suggested that since Fe^{4+} amount decreases by Mo doping, and more electron holes are converted into oxygen vacancies, thus the final electroconductivity of the perovskite is reduced [72]. One can conclude that there must be an optimum level of Mo doping which neither is too low to not be able to protect B-O-B bridges and not too high to reduce all the available possible electron holes.

Another insightful advantage of doping Mo is the significant boosting in carbon tolerance of perovskite. He et al. [78] highlighted the remarkable carbon tolerance of $Sr_2TiNi_{0.5}Mo_{0.5}O_6$. In 2012, Li et al. [79] postulated that the high carbon tolerance of Mo-included oxides like $Sr_2Fe_{1.5}Mo_{0.5}O_6$ is due to two main reasons. First, the higher structural stability induced by Mo doping prevents further metal cluster formations on the surface which hampers enough surface provide for carbon deposition. Secondly, the more oxygen vacancies exerted by Mo doping in an oxide structure are formed just around the active B-site cations like Mo^{6+}. Therefore, the instant formation and consumption of activated carbon species increases the tolerance of the anode towards carbon adsorption.

As another advantage, Lu et al. [70] and Zhang et al. [72] found that Mo doping into $Pr_{0.6}Sr_{0.4}(Fe_{0.8}Ni_{0.2})_{1-x}Mo_xO_{3-\delta}$ and $Pr_{0.4}Sr_{0.6}(Co_{0.2}Fe_{0.8})_{1-x}Mo_xO_{3-\delta}$, respectively, decreased the thermal expansion coefficient (TEC) significantly as Mo dopant was increased. The presence of a high-valent element like Mo in the structure can suppress the reduction in B-site cations (Fe^{4+}, Co^{3+}, Ni^{4+}) to their lower valence states (Fe^{3+}, Co^{2+}, Ni^{3+}) and thus, the TEC is decreasing. As a result, the compatibility between electrode and electrolyte is increased, delaying cracking and failure in the cell during heating or redox cycles.

Despite the sporadically reported benefits of Mo doping into different perovskite structures, and even in LSCF, no studies are available on possible applications of Mo-doped LSCF as anode material in SOFC. It is crucial to note that the advantages of Mo doping are also dependent on the cell design, materials, and thickness of other cell components, electrode microstructure, and even the crystal environment around Mo ions.

1.9   Innovative Processing Methods

Along with the design and selection of materials, the choice of suitable fabricating methods for anode, electrolyte and cathode is noticeable as well. As mentioned before, to realize a biogas-fed SOFC

working at low-intermediate temperatures, a cathode-supported cell with a thin electrolyte and anode layer is preferred. There is a body of research investigating the most efficient and cost-effective methods for SOFC fabrication towards lowering temperature.

Colloidal Processing and Co-sintering

A practical movement towards lowering the temperature is to develop novel and more efficient methods to fabricate thin-film SOFC component layers. Tape casting and screen printing are the simplest and most robust thin-film fabrication methods, with the capability to produce layers of thickness as low as 5 µm [37]. Many researchers have focused on improving the processing and sintering of such thin-film layers with the approach to LT-SOFC applications. The key to understanding ceramic processing is to know the dependency of different steps and to figure out the final relationship between them. Moreno [80] introduced critical remarks about colloidal processing, which is fundamentally the dispersion of powders in a liquid. It plays an important role in the manufacturing process, which is even scalable to large industrial systems. Colloidal processing can be used from powder synthesis to fabrication of thin green tapes. The most important aspect to consider in colloidal processing is to retain and control the interparticle forces during the process, such that the most homogeneity and even microstructure can be achieved.

Sintering is the last step in processing, which can be done in conventional or novel methods: ultrafast high-temperature sintering, cold sintering, or flash sintering. Co-sintering is not as novel as the mentioned methods, but since it shortens the sintering time and energy cost, thus facilitating the fabrication process, has the potential to be improved as an innovative sintering method. Co-sintering can be used to sinter bi-layers simultaneously on a rigid support. Thus, it is important to adjust the sintering heating rate and target temperature, the layers thickness and shrinkage differences between two layers [81]. Sglavo et al. [82]–[84] have worked for many years on increasing the mechanical reliability of thin ceramic layers and investigating the residual stresses and fracture toughness as well as their sintering and

densification, through controlling the processing steps. Stresses are generated upon sintering due to different TEC and sintering kinetics which then lead to the formation of flaws, defects, delamination, retarded densification, or warping. A curvature is created usually due to a mismatch in shrinkages/shrinkage rates. To reduce the developing curvature, a dead load is used on top of the bi-layer upon sintering [85].

1.10   Tape Casting

One of the most widely used industrial processes for manufacturing large-scale thin ceramic sheets and multilayers is tape casting [86]. First, a slurry is prepared from ceramic powders and then it is poured into a stationary device made of a reservoir and blades. The blades that are called "doctor blades" can control the thickness of the tape. There is a moving tape carrier, on which the slurry is deposited from the stationary reservoir [87] (Figure 1.8). To attain high-quality tapes, industrially validating continuous production, the tape casting process should be regulated for the desired final microstructure, in three steps: 1) slurry preparation, 2) casting conditions and, 3) drying [88].
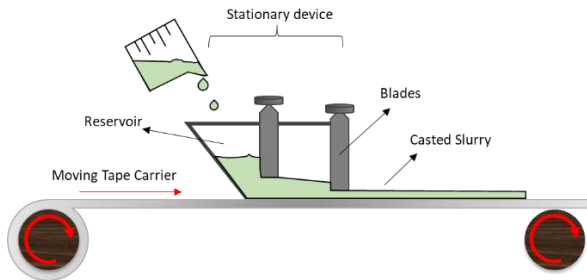
Figure 1.8 Tape casting schematic

1.10.1   Slurry Preparation

Slurry preparation is the most fundamental step. The slurry composition and formulation determine the final microstructure and

thus, the sintering properties of ceramic tapes. To prepare tape casting slurry, the ceramic powder and dispersant are mixed in the solvent in the first step, which is followed by the addition of the plasticizer and binder in the second step [89]. It is important to adjust solid loading concerning the desired thickness of the tape, the intended microstructure, and the sintered properties. Another determinant in slurry processing is regulating the plasticizer-to-binder ratio.

i.   Solvent

While using organic solvent-based suspensions is a common practice in the industry due to simpler deflocculation, lower latent heat, and less energy-intensive drying [90], using water-based tape casting can not only significantly reduce the risks to the environment and human health [91] but also lower the costs associated with installation and the disposal of organic waste [92]. But the biggest issues in the industrialization of water-based tape casting are constrained rheology, slower drying, larger binder amount for a good cohesion and slurry flocculation which make it challenging to control the tape thickness, homogeneity, and flexibility [93][94].

ii.   Solid Loading

Having established that better electrocatalytic activity towards the ORR can be achieved with a more porous cathodic layer, solid loading can be increased up to a point to let enough porosity formation in the layer. On the other side, with very low solid loading, attaining thick supporting layers is not an easy job [95]. In this study, two different solid loadings, 47 wt% and 60 wt% were selected to be examined.

iii.   Plasticizer

The addition of a plasticizer can reduce the suspension viscosity by settling down between the binder polymers and thus, decreasing van der Waals forces. Secondly, they can increase flexibility by lowering the glass transition temperature after casting. Thirdly, they can reduce the shrinkage stresses during drying, which can suppress the cracks and defects, which is of importance specifically in the case of aqueous

suspensions [96]. The plasticization effect is dependent on the plasticizer's molecular weight (M_W) and on its functional groups. Smaller plasticizers benefit from better mobility inside the suspension and thus can induce more flexibility [97]. Slurry preparation is easier and less challenging using low M_W plasticizers, but the following casting and drying steps should be carried out with more prudence. Using a low M_W plasticizer is accompanied by a high degree of plasticization but with very poor mechanical strength in the final green tape. However, a high mechanical strength is a requisite in the processing and fabrication of multilayer ceramics [98], like a SOFC. To achieve high-quality green tapes with enough flexibility and at the same time, with sufficient mechanical strength, there are two solutions: the amount of low M_W plasticizer should be optimized precisely to the binder to attain an optimized Tg, or as another solution, a high M_W plasticizer could be added that can exert mechanical strength as well as flexibility due to its long polymeric chains. This results in lower drying shrinkage as well as simpler tape removal from the carrier as well. Less volatility and lower migration are other advantages of using high M_W plasticizers which end with a smoother and more even tape surface after drying [99]. In addition to that, this helps green tapes by having more open porosities after drying and then sintering, which leads to a high specific surface area as well [100]. However, high M_W plasticizers are less compatible and less soluble in binder polymers due to fewer hydrogen bonds that can be formed between the plasticizer and binder polymers [101]. Furtherly, these two can lead to phase separation, delamination in multilayer ceramics or poor processing.

1.10.2 Casting Parameters

Regardless of the material, casting parameters can affect the thixotropic behavior of the slurry and control the final thickness. As mentioned before, keeping with a constant thickness during continuous industrial casting demands more accuracy in monitoring

the process. The blade gap, the speed of the moving blade and the slurry height in the reservoir are the most essential parameters in controlling the final thickness of cast tapes [102]. Due to the slurry height drop in front of the blade and the resulting decrease in hydrostatic pressure for the slurry flow under the blade, the tapes' thickness reduces as the blade passes over them [102], even though using two parallel blades can reduce the pressure gradient below the moving blades. However, still on a laboratory scale, where the reservoir is not filled in continuously, two blade gaps should be adjusted carefully to reduce the pressure gradient as much as possible during casting, to achieve more uniform particle alignment and thickness over the tape [103]. The speed of the blade moving over the slurry and the blade gap should be adjusted regarding the solid loading and the final desired thickness of green tape [104].

1.10.3 Drying

The drying process consists of two main stages and its rate is regulated by controlling the rate of the following reactions [105]:

$$H_2O \; (surface \; liquid) \\ \leftrightarrow H_2O \; (Vapor) + \; vacant \; site \quad (water \; Evaporation) \quad (1.12)$$

$$H_2O \; (bulk \; liquid) + \; vacant \; site \\ \rightarrow H_2O \; (surface \; liquid) \; (water \; Diffusion) \quad (1.13)$$
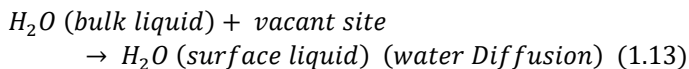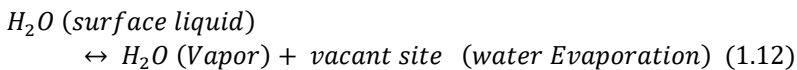
i. Constant Rate Period (CRP)

The first stage in tape drying is called the constant rate period (CRP) since the drying rate is independent of time at this stage but is predominated by the kinetics of water evaporation at the surface. Therefore, the drying rate can be controlled by the relative humidity at this stage, but organic additives have little impact [106]. The initial reaction rate (R_1) is directly related to the flow rate of water vapor (j_{LV}) across the boundary layer above the tape and the relationship is given by [105]

$$R_1 = k_1 \left[H2O_{(Surface\ Liquid)} \right] \quad k_1 = \frac{j_{LV}}{d\left[H2O_{(Surface\ Liquid)} \right]} \qquad (1.14)$$

where k_1 is the evaporation rate coefficient at a specific temperature. Assuming a constant value (H) covering the effects of temperature, surface geometry and air velocity above the surface [107], j_{LV} only varies as a function of ΔP as

$$j_{LV} = H\ (P_{Sat} - P_V) \qquad (1.15)$$

where, P_V is the partial vapor pressure of ambient air above the boundary layer, and P_{Sat} is the saturation vapor pressure of the boundary layer that is in equilibrium with the top surface of the body. The evaporation rate can be controlled by controlling P_V since the meniscus' radius is fixed in S1 and P_{Sat} is constant.

ii.   Falling Rate Period (FRP)

Approaching the end of CRP, the shrinkage stops, and the water meniscus is driven into space between the particles. The capillary pressure decreases, and the water flux slows down abruptly. Due to the fast fall in the rate of drying, the second stage is named the falling rate period (FRP) [108]. In FRP, following the decrease in bulk water, solids and polymers get more concentrated. Therefore, the type, length and quantity of polymer chains in the plasticizer can be crucial in this stage [106]. Any obstruction or hydration in the water pathway to the surface impacts the activation energy for water diffusion and its coefficient rate (D).

Figure 1.9 shows how water molecules can be obstructed by ether oxygens on PEG chains that tend to establish hydrogen bonds with them. In addition to obstruction, the diffusion rate of water molecules hydrated to hydroxyl head groups is constrained by the diffusion rate of PEG chains. The drying rate in FRP (R_2) is proportional to D as

$$R_2 = k_2 \left[H2O_{(Bulk\ Liquid)} \right] [vacant\ site] \quad k_2 = D \qquad (1.16)$$
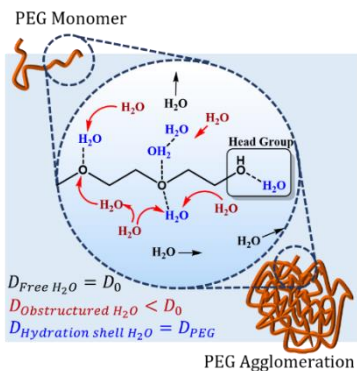
Figure 1.9 Water diffusion coefficients in a suspension with PEG polymers

where D is defined as

$$D = \left[\frac{1}{1 + (\emptyset/2)}\right] D_0 \, P_f + D_b \, P_b \qquad (1.17)$$

where $\emptyset$, P_f and P_b are the fraction of obstructed, free and bounded water molecules, respectively, D_0 is the self-diffusion coefficient and D_b is the diffusion coefficient of bounded water which is almost the same as the PEG [109]. PEG 4000 long chains can form bigger assemblies and larger $\emptyset$, besides thicker hydration shells and larger P_b as well. Thus, D is more reduced and FRP slows down more by PEG 4000 than by a low M_w plasticizer. This gives solids and polymers adequate time for rearrangement makes the body dry uniformly and the particles in the tape settle in a well-packed manner.

1.10.4 Plasticizer to Binder Ratio

To increase SOFC durability, a careful choice of components for electrodes should be made. However, choosing the right component is not the only factor. Adjusting the composition during colloidal processing is equally important in optimizing the final microstructure and fulfilling the desired properties [110] [111]. Adjusting the

plasticizer-to-binder ratio is one of the main determinants in tape casting processing to achieve high-quality green tapes. Thus, it can significantly affect the final microstructure and the redox stability of components after sintering. The **R-value** introduces the ratio of compatibility between the plasticizer and the binder, and it is defined in terms of weight percentage as $R = (plasticizer/binder) \times 100\%$ [112].

i. Plasticizer to Binder Ratio Effect on Microstructure

The final porosity in tapes depends on the packing of solid particles inside the matrix of binder and plasticizer [113]. To lessen internal and residual stresses in electrodes during lamination and after heat treatments, the layers should benefit from more symmetrical properties and the in-plane anisotropic shrinkage of green tape needs to be constrained as much as feasible [114]. Anisotropic particles or polymers can lead to orientated pores after sintering as well as anisotropic microstructure [115]. An anisotropic factor $K_{(L, P)}$ can be defined by

$$K_{(L, \ P)} = 100 \left(1 - \frac{\varepsilon_L}{\varepsilon_P} \right) \quad Anisotropic \ Factor \quad (1.18)$$

where ε_L and ε_P are the longitudinal and perpendicular shrinkage strains in the tape after sintering. This definition states that when there is larger longitudinal shrinkage, $K_{(L, P)}$ is negative [116].

When the particles are more spherical and isotropic, the molecular weight of polymers, the interaction between plasticizer and binder and thus, the plasticizer-to-binder ratio can shape the final porosity and microstructure, and regulate the anisotropicity [117]. Although previous studies showed only a small impact of R-value on packing density [118], some recent works proved that the solid density and microstructure after sintering are influenced largely by R-value. J. Li

et al. [119] confirmed that changing the plasticizer (DBP[1]) to binder (PVB[2]) ratio can improve the final microstructure and sintering performance of a glass-ceramic composite fabricated by tape casting. Another work by Y. Duan et al. [120] showed that the density and solid packing are influenced by the plasticizer (BBP[3]) to binder (PVB) ratio in tape casting of silicon nitride substrates. Zeng et al. [20] proved that increasing R-value in water-based tape casting of B_4C, first decreased the viscosity and then increased it. The least variation in rheology was achieved when R-value was set at 1 wt%. Zhou et al. [21] showed the residual porosity in green tapes was affected by R-value, which then influenced the microstructure, compressibility and strength.

ii. Plasticizer to Binder Ratio Effect on Redox Stability

As mentioned before, one of the main issues in employing lanthanum ferrite as the electrode in SOFC is considering the redox stability under reducing and oxidizing conditions. In addition to the composition of perovskite, the processing method can have an impact on the redox stability, through controlling the final particle size and distribution, thus the attained microstructure after sintering [39]. Santaya et al. [121] proved that smaller grain size after sintering promoted more cation segregation on the surface and as a result, the perovskite $SrTi_{0.3}Fe_{0.7}O_3$ was more decomposed.

1.10.5 LSCF Tape Casting

LSCF is one of the most studied perovskite material to be used as a cathode in solid oxide fuel cells (SOFC) or as oxygen transport membrane (OTM) in many mass-production industries, due to its high mixed ionic and electronic

---

[1] DBP: Di-Butyl Phthalate
[2] PVB: Poly Vinyl Butyral
[3] BBP: Butyl Benzyl Phthalate

conductivity, good catalytic activity and high stability towards oxidation, even at low-intermediate temperatures (< 800°C) [122].

Fedeli et al.[123] used organics-based tape casting to create ≈ 700 μm thick LSCF6428 asymmetric membranes. Similar LSCF membranes were also examined by Schulze-Kupper et al. [124] and Serra et al. [125]. Some other researchers, Nie et al. [126] and Liu et al. [127] suggested organics-based tape casting to produce graded LSCF6428 cathodes with a thickness ≤ 50 μm. While using organic solvents in tape casting is a common practice in industry due to their lower latent heat and less energy-intensive drying [90], water-based tape casting can not only significantly reduce the risks to the environment and human health but also lower the costs associated with the installation and disposal of organic waste [91]. Firstly, Middleton et al. [128] cast very thin tapes of LSCF (5–10 μm) using water as the solvent in 2004. Fernandez-Gonzalez et al. [129] fabricated LSCF6428 tapes of 35% solid loading by water-based tape casting with the focus on slurry stability and microstructural evolution at different sintering temperatures. The tapes showed 85% relative density at 1200°C. In another work, Junior et al. [130] produced LSCF1991 asymmetric membranes of 25% solid loading using water as the solvent.

Project Aim

This project aimed at developing a cathode-supported SOFC to be fed directly by biofuels and thus, innovating a coke-resistant material for the anodic catalyst. Two perspectives were considered during cell fabrication: the design and the material.

Concerning the material, the project intends to further develop LSCF by doping molybdenum as an acceptor-type dopant into B-site with the approach to possible anodic applications. LSCFMo powders are going to be produced by the auto-combustion method in this project. The combustion method is used because it can offer a way to produce fine ceramic powders with a more porous and homogenous structure at the end without the requirement for pricy precursors [131]. An enhanced combustion method known as an auto-combustion process can produce extra heat through an exothermic reaction [132]. As a result, the combustion is more complete, and the reaction produces a higher yield.

Regarding the cell design, this study decided on the fabrication of a cathode by water-based tape casting which should benefit from enough porosity, a good balance between flexibility and mechanical strength and a good thickness consistency over the tape. This can guarantee a reliable and promising tape casting process not only on a lab scale but also for massive and continuous industrial manufacturing.

One of the most used plasticizers in tape casting is polyethylene glycol. This study aims at the fabrication of cathode electrodes by water-based tape casting, which benefit from enough porosity, a good balance between flexibility and mechanical strength and a more thickness consistency over the tape which all together can make a reliable and promising tape casting process for massive and continuous industrial manufacturing. The goal is going to be achieved by embedding a high M_W polyethylene glycol, PEG 4000 as the plasticizer into the water-based suspensions of LSCF or LSF.

According to this, the cell diagram follows as LSCFMo|GDC|LSF and its schematic is shown in Figure 1.10.
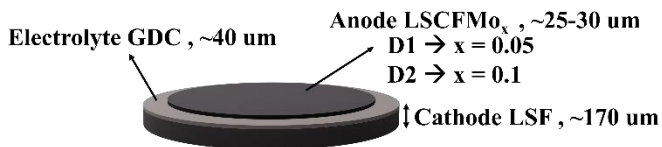
Figure 1.10 Target cell schematic

The SOFC development project is pursued by three main steps, as follows:

I. The first step concerns the synthesis of powders and their characterization.

II. The second step covers the cathode fabrication by developing the tape casting process.

III. The third step regards fabrication of the button SOFC and its characterization, electrochemical impedance, and performance evaluation.

CHAPTER 2

Experimental and Methods

2.1   Powders Synthesis and Characterization

2.1.1   Synthesis

$La_{0.6}Sr_{0.4}(Co_{0.2}Fe_{0.8})_{1-x}Mo_x O_{3-\delta}$ (LSCF (x = 0), LSCFMo5 (x = 0.05) and LSCFMo10 (x = 0.1)) powders were synthesized using an auto-combustion method with an innovative three-fuel system (Figure 2.1). The stoichiometric amounts of metal salt (CARLO ERBA RPE Reagents SRL): lanthanum nitrate hexahydrate ($La(NO_3)_3.6H_2O$), cobalt nitrate hexahydrate ($Co(NO_3)_2.6H_2O$), ferric nitrate nonahydrate ($Fe(NO_3)_3.9H_2O$), ammonium heptamolybdate tetrahydrate (($NH_4)_6Mo_7O_{24}.H_2O$) and strontium nitrate ($Sr(NO_3)_2$, Acros Organics) were dissolved and mixed in 250 ml distilled water in a beaker using a magnetic stirrer until a clear solution was achieved. Ammonium nitrate (($NH_4)NO_3$, CARLO ERBA RPE Reagents SRL) was then added to this mixture as an oxidant aid with 14.5:1 molar ratio to the total metal cations. The fuel components, ethylenediaminetetraacetic acid (EDTA, CARLO ERBA RPE Reagents SRL), citric acid (CH_3COOH, J.T.Baker) and polyethylene glycol (PEG 20000, Alfa Aesar GmbH), were mixed separately in 250 ml distilled water in a beaker with a 1:2:3 ratio to the total metal cations, using the magnetic stirrer. The amount of added ammonium hydroxide ($NH_4(OH)$) to the second mixture was adjusted to reach a solution with 6 < pH < 8. Both mixtures were merged together in a beaker 600 ml, and the new mixture was magnetic stirred at 80 °C on a hot plate, for almost 24 h, until a reddish-brown gel structure was achieved. The gel was then put in a muffle furnace (Nabertherm, Controller P330) pre-heated at 250 °C and a rapid auto-combustion reaction took place resulting in a black ash powder, which was further calcined at 1000 °C for 4 h. For more safety, the beaker 600 ml was put inside an aluminum box in the furnace.
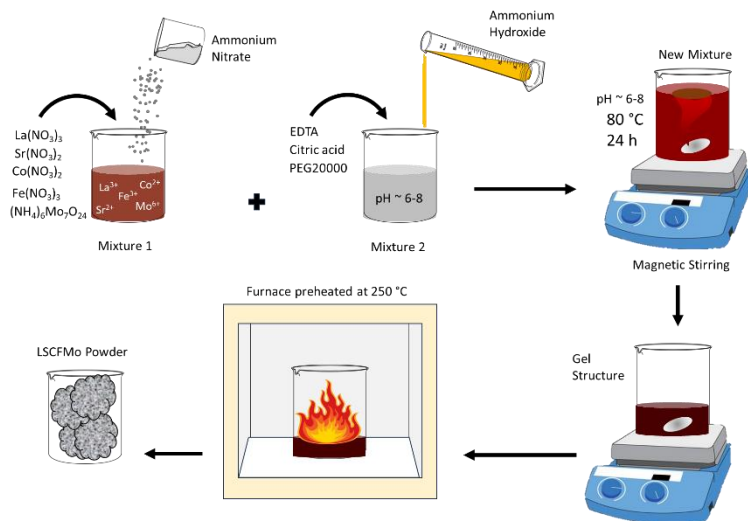
Figure 2.1 Schematic of powder synthesis by auto-combustion method

2.1.2 Characterization

The mineralogical composition of the as-synthesized powder was characterized by X-ray diffraction (XRD) performed by an Italstructures IPD3000 X-ray diffractometer equipped with cobalt and copper anode source; samples are positioned in reflection geometry with a 5° angle with respect to the incident beam. Crystal parameters refinement was carried out by Maud 2.93 using the reference crystallography data files. Powder particle size and morphology were assessed by field-emission scanning microscopy (FE-SEM) using ZEISS® Supra 40 microscope (Carl Zeiss Microscopy GmbH, Jena, Germany).

Subsequent studies investigated the microstructure and mechanical stability of LSCFMo powder under reducing conditions. For these studies, green tapes prepared from LSCFMo were sintered at 1225 °C for 3 h. Then, they were subjected to 5% H_2/Ar gas flow as a reducing agent at 900 °C (heating rate = 5 °C/min) for 10 h. The phase stability of the tapes was assessed by XRD and the mechanical stability was

tested manually. The bulk density of sintered and reduced tapes was evaluated by SEM analysis with the aid of image analysis software (ImageJ 1.54f). The surface porosity of the tape was assessed by proper threshold adjustment of the image and calculating the pixel ratio with respect to the total pixels in the image area.

2.2   Cathode Tape Casting and Characterization

2.2.1   Slurry Preparation and Characterization

The as-synthesized LSCF powder was dry ball-milled for 3 h with zirconia spheres. Water-based slurries with different solid loading and plasticizer amounts were prepared. LSCF powder of 47.0 wt% and 60.0 wt% (corresponding to 17.0 vol.% and 18.5 vol.%, respectively), was dispersed in distilled water using 0.5 wt% of an ammonium polyacrylate dispersant (DARVAN-821A, Mw = 3500, 40 wt% active matter). Corn starch (Carlo Erba S.A.S) was also added up to 10% of the total suspension weight as a pore former to exert enough porosity. The suspensions were mixed using zirconia spheres with the ratio 2:1 to the total mass of LSCF ceramic powders, for 3 h in a Turbula (T2F, WA BACHOFEN AG, CH). Then, the slurry was filtered and de-aired by low vacuum pressure to remove entrapped air bubbles. 0.4 wt%, 0.6 wt% and 0.7 wt% of PEG 4000 solution (20 wt% dry solids) was added as plasticizer and an acrylic latex emulsion (Duramax B1000, 55% active matter, Tg = −26 °C, pH = 9.0–9.8) of 20 wt% and 26 wt% was added as the binder. The weight percentages are considered with respect to the total suspension weight in each step. The mixture was stirred mechanically for 2 h at 150–170 rpm. Table 2.1 lists the composition of the different slurries. The R-value introduces the ratio of compatibility between the plasticizer and the binder, and it is defined in terms of weight percentage as $R = (plasticizer / binder) \times 100\%$ [112]. In this study, two different solid loadings 47 wt% and 60 wt% (corresponding to 17.0 vol.% and 18.5 vol.%, respectively) were investigated, and the binder-to-solid loading ratio was kept constant (23.6 ± 0.2 wt%) in all slurries, to eliminate the effect of binder-to-solid loading ratio and for better comparing the

effect of plasticizer amount. Figure 2.2 shows the schematic of tape casting procedure.
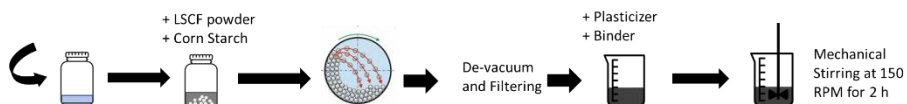
Figure 2.2 Schematic of slurry preparation

The rheology of the slurries was characterized before adding the binder through a Brookfield viscometer (Myr rotational viscometer VL2, Viscotech Hispania, s.l.). The sample temperature kept constant at 21 °C. The viscosity was determined at different shear rates in the range of $0.06–2.80 \ s^{-1}$, by increasing the rotation speed from 0.2 rpm to 10 rpm. The final values were recorded after around 10 revolutions.

2.2.2 Casting and Sintering

In this study, a laboratory-scale tape casting machine was used as shown in Figure 2.3. In contrast to industrial-scaled tape casting, a moving device, made of a reservoir and two parallel blades, was used over a fixed polyethylene terephthalate (PET) tape carrier.
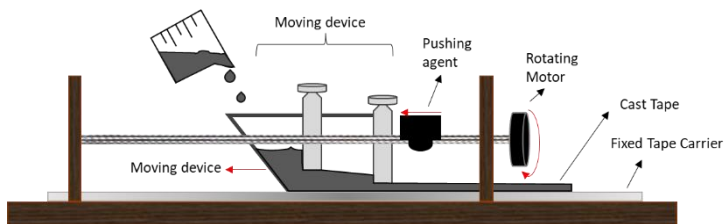
Figure 2.3 Schematic of lab-scaled tape casting machine

Each prepared slurry was poured into the reservoir and the blade gap was adjusted at 900 μm. The casting was carried out at speed of ~10 mm/s. The cast layers were dried within the closed chamber for 48 h at two relative humidities (RH), 35% and 70%. Then, the dried green tapes were cut and sintered through a two-stage program in a high-temperature furnace (Nabertherm, ProgramController C42), the

first up to 380 °C (1 h dwell time, heating rate = 0.5 °C min^{-1}) and the second up to 1200 °C (3 h dwell time, heating rate = 3 °C min^{-1}).

2.2.3 Tapes Characterization

Surface morphology and defect development on green tapes were observed using an optical microscope.

The compromise between the flexibility and mechanical strength of the green tapes was determined by the tensile strength test using a universal mechanical testing machine Instron 5969 (Instron, Norwood, MA), equipped with a 100 N load cell. The test was performed on 1BA specimens (Standard ISO 527)) and the stress-strain curves were measured according to standard ASTM D 638–08. Samples with a gauge length of 40 mm, width of 5 mm and grip width of 10 mm were placed under tension using a crosshead speed of 5 mm/min. The yield strength (σ_y) was calculated by constructing a parallel line offset by 0.2% strain to the linear stress-strain line. The ultimate strength (σ_u) was found as the maximum point in the stress-strain diagram. The elastic modulus (E) was found by averaging the tangents between any two consecutive points in the stress-strain diagram, up to σ_y. The flexibility quality was also judged by the elastic modulus and the minimum bending radius of the tapes. A tape with a bending radius lower than 3 mm was supposed flexible in this study.

Eight disk samples taken from various locations on each green tape were used to assess the in-plane and thickness shrinkage as well as the weight loss during sintering to examine the consistency and homogeneity. The relative standard deviations (RSD) were plotted on a radar chart using the statistical analysis of these values, and the centroids of the curves were computed. The tape consistency was evaluated using the centroid's distance from the plot's origin.

Sintered LSCF tapes at 1200 °C were investigated in terms of density and microstructure. Using Archimedes' approach, the relative density and apparent porosity of sintered tapes were calculated using the theoretical density of LSCF (6.321 g cm^3). The sintered tape surface was observed by field emission scanning electron microscopy

(FESEM). The green tapes' shrinkage and anisotropicity during sintering were measured based on dilatometric measurements. The dilatometry analysis was performed on 10 x 20 mm^2 rectangular bar samples, which were cut off the tapes and rolled along and transverse to casting directions, using a horizontal alumina dilatometer (Linseis L75, Germany) with a heating rate of 3 °C min^{-1} up to 380 °C and 5 °C min^{-1} up to 1200 °C.

The composition of the sintered tapes was determined by XRD while they underwent reduction and oxidation cycles to examine their phase stability under reducing and oxidizing conditions. Sintered disks were heated to 900 °C (heating rate: 3 °C min^{-1}) while being subjected to reducing and oxidizing environments for 10 h. As reducing and oxidizing agents, 5% H_2/Ar and pure air gas were utilized, respectively. For safety purposes, N_2 and air were purged into the furnace for 5 min before each cycle.

2.3   SOFC Fabrication

2.3.1   Half-Cell

LSF commercial powder (La$_{0.8}$Sr$_{0.2}$FeO$_{3-\delta}$: LSF20, BET = 9.7 m^2/g, NexTech Materials) with spherical particles of 40–500 nm diameter (d$_{50}$ = 250 nm and d$_{90}$ = 200 nm), was used to fabricate the cathode layer. The same tape casting procedure as LSCF was used to prepare the LSF tape. LSF ceramic powder was added up to 47 wt% (17.0 vol.%) solid loading. R-value was optimized at 1.00 wt%, similar to the slurry 4706 composition. The LSF casting was carried out with the blade gap of 900 μm and casting speed around 10 mm/s. The tape was dried at RH = 70% after 48 h.

GDC commercial powder (Ga$_{0.9}$Ce$_{0.1}$O$_{1.95}$: GDC10, BET = 10–15 m^2/g, d$_{50}$ = 700 nm, d$_{90}$ = 60 nm, NexCeris, OH) was used to prepare the electrolyte layer, using the same tape casting procedure but with different composition and casting parameters. The solid loading of GDC ceramic powder was set at 70 wt% (23.5 vol.%). No plasticizer was added for electrolyte preparation, but the acrylic latex emulsion

(Duramax B1000, 55% active matter, Tg = −26 °C, pH = 9.0–9.8) was added as binder at 15 wt% with respect to the total suspension weight. Then, GDC slurry was cast on a PET carrier using a blade gap of 80 μm and with moving speed of around 20 mm/s. The relative humidity in the chamber was controlled at 70%. The cast tape was dried after 24 h. The slurry composition details are shown in Table 2.1 for both the cathode and electrolyte layers.

Then, GDC and LSF green tapes were laminated together by a Carver hydraulic thermopress (conditions = 20 MPa/ 75 °C/10 min) to produce the GDC|LSF half-cell.

Table 2.1 Water-based slurry composition (wt%)

Slurry label	Solid loading wt%	Plasticizer wt%	Binder wt%	Dispersant wt%	Pore former wt%	R-value	Binder / solid loading
		PEG 4000	Duramax B1000	DARVAN 821A	Corn starch		
LSCF Cathode							
4707	47	0.7	20	0.5	10	1.27	23.4
4706		0.6				1.09	
6006	60	0.6	26			0.84	23.8
6004		0.4				0.56	
LSF Cathode							
	47	0.7	26	0.5	10	1.00	
GDC Electrolyte							
	70	–	15	0.8	–	–	

2.3.2 Anode Coating

To coat the anode, LSCFMo ink was screen-printed onto the GDC side of the half-cell previously realized. To prepare the screen-printing ink, a vehicle of 94 wt% α-terpineol as the solvent and 6 wt% ethyl cellulose (EC) as the binder was prepared. The synthesized LSCFMo$_x$ (x = 0.05, 0.1) powder was added to the vehicle to reach 27 wt% solid loading. The mixture was mechanically stirred for 1 h and then, an

octyl phenol polyethoxylate surfactant (Triton-x100, Sigma-Aldrich Co., St. Louis, MO, USA) was added up to 7 wt% of the powder. The ink was screen printed using a manual screen-printing machine (Gabrielli Technology s.r.l.) onto the GDC layer through a circle stencil with 10–20 mm diameter and 250 mesh.

2.3.3 Co-Sintering

Considering the sintering shrinkage of the half-cells disks with a diameter of 12–24 mm with printed anode at the center were produced. The green button-cells were co-sintered with a two-stage sintering program, the first step at 600 °C for 1 h (heating ramp = 0.5 °C/min) and the second one at 1225 °C for 3 h (heating ramp = 2 °C/min), while a dead load was applied to equalize the warping during sintering.

2.4.1 Cell Characterization

The microstructure of anode and cathode surfaces and the cross-section morphology of the cells were observed by SEM. The porosity is assessed by ImageJ software (1.54 f).

Electrochemical measurements including open circuit voltage (OCV), polarization curves (current-potential, I-V curves), impedance spectroscopy (EIS) and galvanostatic measurements were performed in temperature range 600–800 °C, using a BioLogic diagnostic tool equipped with a 100 A booster and frequency response analyzer module for impedance spectroscopy. Controlling the temperature was done using a thermocouple attached to the cathode. The quality of outlet gas was verified inside Thermostar® equipment (from PFEIFFER Vacuum) capable of measuring masses up to 300 amu.

To carry out the electrochemical and performance measurements, each produced cell was mounted on an alumina tube using a ceramic paste (Aremco) for sealing gas fuel on the anodic side. The cathode side was exposed to static airflow. Gold wires and paste were applied to both electrodes serving as electrical current collectors. SOFC open

circuit voltage (OCV) measurements were carried out at 600 °C at a total flow rate F = 50 cm^3/min in three stages. A pre-treatment of the LSCFMo anode was performed using an inert He (50 cm^3/min) gas flow for the time necessary to ensure that the OCV was stable and to clean any organic residue derived from sealing paste or gold decomposition off the anodic tube. Then, the cells were fed first by dry biogas (30 cm^3/min CH$_4$ + 20 cm^3/min CO$_2$) and then by pure methane (50 cm^3/min). The cells were fed by liquid methanol fed using a syringe pump and He as a carrier (0.5 cm^3/ h CH$_3$OH + 25 cm^3/ min He) at 600 °C, to understand the mechanism and compare the catalytic activity towards the fuel oxidation. To examine the effect of He carrier on methanol oxidation, two amounts of He flow rate (10 and 50 cm^3/ min) were tested. Short-term durability tests were carried out at 600 °C with methanol and at 700 °C with both H$_2$ (50 cm^3/ min) and methanol as fuels, under galvanostatic conditions. Electrochemical impedance spectroscopy (EIS) measurements and polarization curves (current-potential I-V curves) were examined. Carbon presence on the anode side was evaluated optically.

Figure 2.4 illustrates the schematic procedure of realizing the whole button-cells in summary.
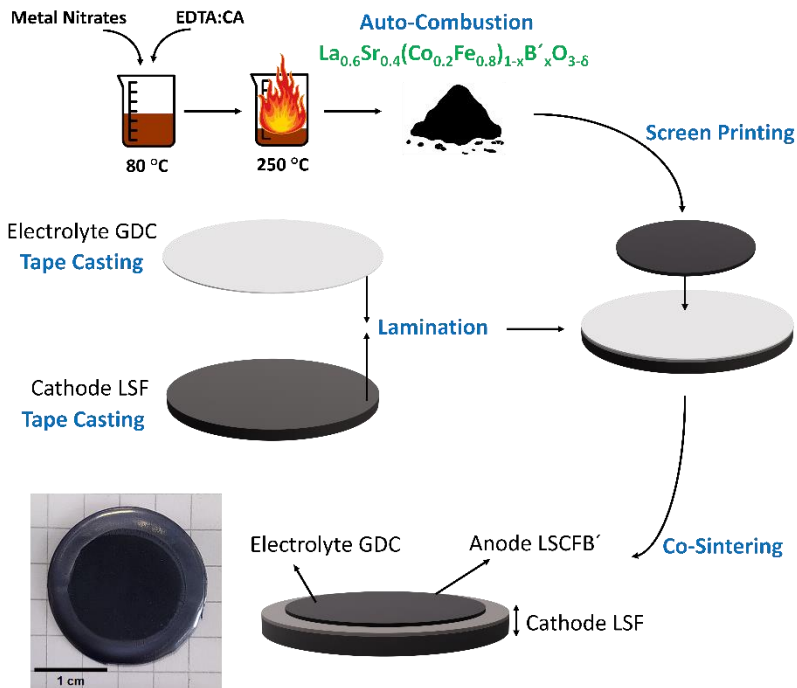
Figure 2.4 Schematic of button-cells fabrication procedure

CHAPTER 3

Results and Discussion

I. STEP 1: Powder Characterization

3.1 Phase Composition and Morphology

By using PEG 20000 in addition to EDTA and citric acid as fuel, the modified auto-combustion process was effectively used to create $LSCFMo_x$ (x = 0, 0.05 and 0.1) powder. The relatively stable chelation of metal cations in solution by EDTA and citric acid is another factor contributing to the slow combustion. In the current study, the polymer PEG 20000 was used to increase combustion intensity, which resulted in pure phase production. This is so that non-chelated cations can be trapped inside the shell of a kind of micelle rather than via covalent bonding, which is how PEG and other polymeric fuels create complexes with them. The metal cations that are so chelated can be reduced more quickly due to weak interactions with polymeric chains. This will compensate for the less intense combustion of citric acid and raise the yield [133], [134].

Figure 3.1a shows the Rietveld-refined XRD pattern of the produced powder and it is verified the phase $La_{0.6}Sr_{0.4}Co_{0.2}Fe_{0.8}O_{3-\delta}$ formation in excess to 98% purity. The porous network microstructure with particle sizes ranging from 150 to 200 nm is shown in Figure 3.1b. The XRD results in Figure 3.2a show the phase pure rhombohedral $LSCFMo_x$ structure. The peaks shift further towards lower angles by increasing the Mo dopant in the B-site. This is because of larger ionic radii of Mo^{6+} (0.59 Å) compared to Fe^{4+} (0.58 Å) and Co^{4+} (0.53 Å) and because Fe^{4+} and Co^{4+} are partially reduced to Fe^{3+} and Co^{3+} following Mo doping, to fulfil the electroneutrality in the structure [72]. In LSCFMo10 synthesized powder, 5 wt% $SrMoO_4$ is detected as impurity which indicates that Mo could not be entirely doped into B-site.
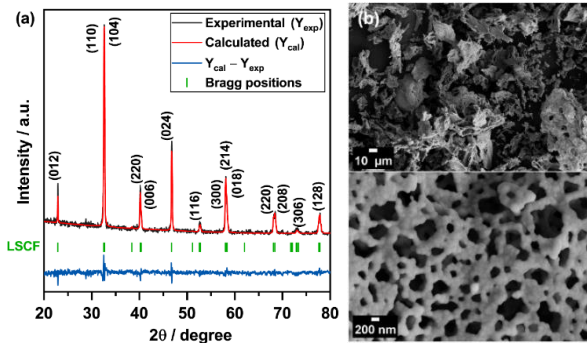
Figure 3.1 a) XRD Rietveld refinement, and b) porous microstructure of the synthesized LSCF powder

The real Mo dopant amount in the structure was found to be around 8% instead of 10%, using peak analysis Maud software. This indicates that Mo could not be doped completely into B-site and is assumed to be the result of pH variations during powder synthesis. At lower and higher pH, cations' oxidation state changes and this hampers their participation in the formation of the desired crystal structure [135]. Figure 3.2b, c illustrates the results of an electron microscopy study of LSCFMo5, which indicates an extremely porous powder morphology with particles ranging in size from 50 to 200 nm. The morphologies of LSCF and LSCFMo10 are the same.
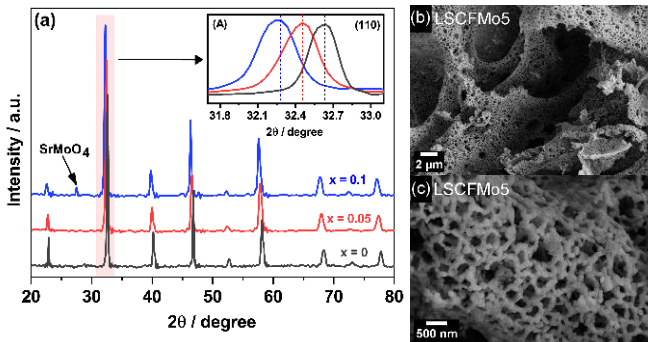
Figure 3.2 a) XRD spectrum of as-synthesized $LSCFMo_x$ (x = 0, 0.05, 0.1) powders with the corresponding b, c) FESEM images

II.   STEP 2: Cathode Tape Casting

3.2   Slurry Rheology

The rheological behavior of the slurries prepared with different amounts of LSCF powder and plasticizer was investigated. The measured viscosity is more precise at high shear rates due to the lower full-scale viscosity range for the chosen spindle and increased measured torque.
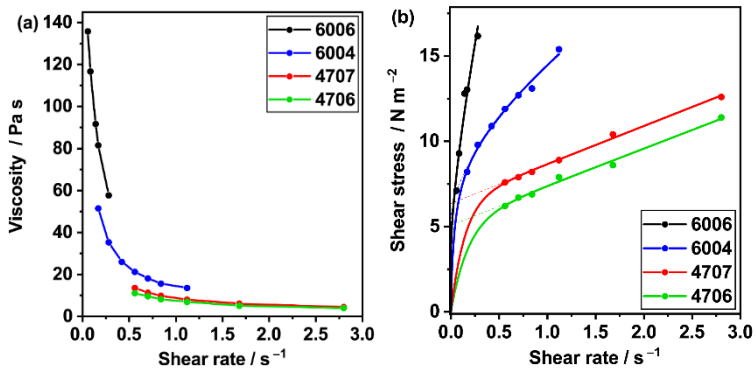
Figure 3.3 Rheological behavior of the slurries in a) viscosity-to-shear rate and b) shear stress-to-shear rate plots.

Figure 3.3a shows that the viscosity always increases as the shear rate decreases, in a typical shear-thinning behavior which is more evident at higher solid loading and plasticizer content. At the highest shear rate (2.8 s^{-1}), the viscosity is independent of the polymer amount, but the effect of PEG 4000 load on viscosity is only evident at a lower shear rate. Figure 3.3b shows the flow curves fitted according to viscoplastic models. A high viscosity was observed at low shear rates, which follows an exponential growth up to a yield point and then, decreased by a shear-thinning behavior. The flow curves of the slurries with 47 wt% (17.0 vol.%) solid loading were better fitted with the Bingham-Papanastasiou model following the equation:

$$\tau = \left(\mu_B + \frac{\tau_y}{|\dot{\gamma}|}[1 - \exp(-m|\dot{\gamma}|)]\right)\dot{\gamma} \qquad (3.1)$$

where τ is shear stress at a specified $\dot{\gamma}$ shear rate, τ_y the yield stress and μ_B the yielding viscosity. After the yield point, the slurries 4706 and 4707 show Newtonian behavior due to the high amount of water. However, the difference between 4706 and 4707 slurries is in the yield point above which the viscosity changes from yielding (as a result of PEG 4000 agglomerations) to the unyielded one (when PEG 4000 chains elongation takes place). Due to more PEG 4000 amount and larger agglomerations at low shear rates in the slurry 4707, it shows a higher yield point before flowing freely. The parameter (m) depends on the intrinsic properties of the suspension and has the dimension of time, which determines the exponential growth rate of viscosity below the yield point. This model applies to all yielded and unyielded regions of the slurry. Above the yield point, the slurries with 60 wt% (18.5 vol.%) solid loading exhibit non-Newtonian behavior. The Herschel-Bulkley-Papanastasiou model provided a better fit for the slurry 6004 following the equation:

$$\tau = \left(k|\dot{\gamma}|^{n-1} + \frac{\tau_y}{|\dot{\gamma}|}[1 - \exp(-m|\dot{\gamma}|)]\right)\dot{\gamma} \qquad |\tau| > \tau_y \qquad (3.2)$$

, where k is consistency, and n is the shear-thinning constant. However, the slurry 6006 showed a more gradual transition to the unyielded zone and its viscosity better matched the Casson-Papanastasiou model as

$$\tau = \left(\sqrt{\mu_C \dot{\gamma}} + \sqrt{\tau_y}[1 - \exp(-\sqrt{m\dot{\gamma}})]\right)^2 \qquad |\tau| > \tau_y \qquad (3.3)$$

, where μ_C is the yielding viscosity. This model is supported by the observation that long polymeric chains, such as PEG 4000 chains, can modulate viscosity by varying their elongations in response to applied stresses [102].

At low shear rates, even a slight increase in the polymer amount, particularly those with long polymeric chains like PEG 4000, causes the viscosity to rise exponentially. This may explain why the amount of long polymeric chains in the slurry has a large impact on the parameter (m). As opposed to this, high shear rates cause polymeric

chains to lengthen longer which lowers the viscosity and facilitates the flow. After tape casting and upon releasing the blade load, the shear rate approaches zero, followed by an increase in friction and shear stress. This can gradually hamper the mobility and sedimentation of ceramic particles. Thus, shear-thinning behaviour favours the achievement of homogenous green tapes by preserving the viscosity for a longer time and limiting the slurry flow, especially at the edges after casting [102]. After drying, tape 6006 shows more homogeneity of particle distribution and less sedimentation.

3.3 Defects and Stress Development

Defective and nearly defect-free green tapes were produced at room temperature and relative humidity levels of 35% and 70%, respectively. All green tapes were able to attain a total effective area of 15×25 cm^2, and their dried thicknesses were roughly 330 μm for 60 wt% (18.5 vol.%) solid loading tapes with 63.3 % drying shrinkage, and 240 μm for 47 wt% (17.0 vol.%) solid loading tapes with 73.3 % drying shrinkage. Based on the observed defects, two significant factors influencing the quality of the tapes were determined. First, the relative humidity and, second, the compatibility between Duramax B1000 (binder) and PEG 4000 (plasticizer).

3.3.1 Effect of Drying Conditions

At RH = 35%, P_V is significantly lower than P_{Sat} and, as a result, j_{LV} is so rapid that water at the surface evaporates more quickly than it diffuses toward the surface. A crust layer forms on the top surface of the body. At this moment, P_{Sat} is very close to zero thus j_{LV} is rapidly decreasing. The trapped vapour must be squeezed out of this crust layer for the water to continue to evaporate. As a result, the surface of tapes cast at RH = 35% develops crow's foot cracks (Figure 3.4a). By doubling the relative humidity from 35% to 70% within the drying chamber, more uniform and crack-free tapes are produced as a result of the surface evaporation rate decreasing and approaching the bulk water diffusion rate (Figure 3.4b).
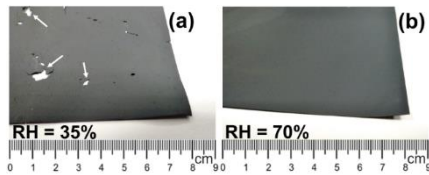
Figure 3.4 Tapes drying at a) RH = 35% and b) RH = 70%

3.3.2   Effect of Plasticizer to Binder Ratio

Figure 3.5 shows hydrogen bond interactions between PEG 4000 and Duramax B1000, but due to PEG 4000's lengthy polymeric chains, its compatibility and solubility with Duramax B1000 are constrained.
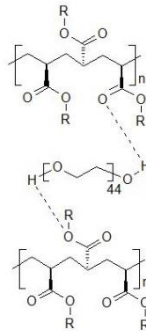
Figure 3.5 Duramax B1000- PEG 4000 interaction during mixing

Figure 3.6 illustrates how different R-values affect the final surface morphology of the green tapes. The organic additives, which will be removed during the sintering process' de-binding step, reflect the beam in the lighter areas. PEG 4000 is added up to 1.09–1.27 wt% of Duramax B1000 in tapes 4707 and 4706. Numerous "raindrop" flaws can be seen on tape 4706, with more severe flaws of the same kind on tape 4707. Because of PEG 4000's lengthy polymeric chains, the

excess quantity outside the range of compatibility with Duramax B1000, which can even occur at extremely low concentrations (<0.2 wt%), aggregate and lead to phase separation [136]. Furtherly, PEG 4000 agglomerations are squeezed out near the conclusion of FRP as a result of drying shrinkage, leaving "raindrop" flaws on the surface. The holes in tape 4707, which has a higher R-value, are deeper and more severe than the tape 4706, expectedly.

In tape 6004, the PEG 4000 quantity is less than adequate to completely cover the gap between Duramax B1000 polymers, with the lowest R-value = 0.56 wt%. Duramax B1000 is a low Tg (−26 °C) acrylic component that also contributes to the tape's flexibility at ambient temperature [137]. Flat, crack-free tapes are produced as a result. However, the extra binder and its accumulation on the tape's surface, denoted by light areas, leave the tape surface sticky after drying [112]. In tape 6006, PEG 4000 is embedded almost entirely within Duramax B1000 polymers with R-value = 0.84 wt%, resulting in a homogenous tape with evenly dispersed polymers and particles. The flexibility induced by a high Mw plasticizer such as PEG 4000 can counteract shrinkage forces enough, such that limit the development of stresses and further fractures. Due to the appropriate R-value, after the tape had dried, nothing left of any extra PEG 4000 or Duramax B1000 can be seen on the surface. The tape 6006 is produced flat, with a perfectly smooth and opaque surface that avoids any flaws or cracks.
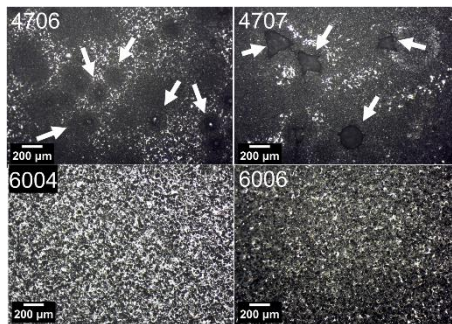
Figure 3.6 R-value effect on green tape morphology

3.4 Tensile Strength and Flexibility

The green tape peeling-off force and rolling property rely on the balance between flexibility and mechanical strength, as well as adhesion between the tape and carrier, which is linked to the R-value. To ensure continuous tape removal and rolling in the industry, the plasticity in the tapes should be optimized to elasticity [138]. The minimum bending radius for the tapes is shown in Figure 3.7, which decreases with R. Two tapes (4707 and 4706) show a higher bending radius, while tape 6004 is considered overly flexible. Extra Duramax B1000 may also impact the plasticizing effect. The tape 6006 aims for perfect flexibility and easy handling, with a minimum bending radius of 2.57 mm.
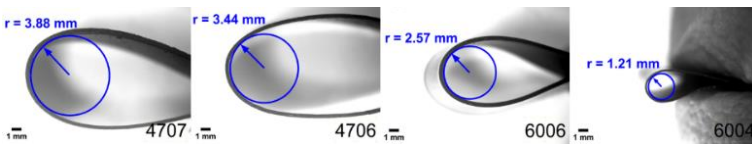
Figure 3.7 Minimum bending radius in tapes with different R-values

The stress-strain curve for tapes under tensile stress is shown in Figure 3.8, supporting the findings of bending radius measurements. As the R-value drops, yield strength decreases, and the plastic deformation range expands. The least plastically deformed tapes, 4707 and 4706, only slightly break after yield stress. Tape 6004 with the lowest R-value requires more effort to remove, resulting in more distortion and stretch. Tape 6006 demonstrates an excellent balance between mechanical strength and flexibility, allowing easy removal and rolling without damage. Its elastic modulus, $E = 1.1$ MPa, indicates a stored strain proportionate to the applied stress, ensuring a strain capacity that is neither too high to permanently distort the tape nor too low to prevent tension release.
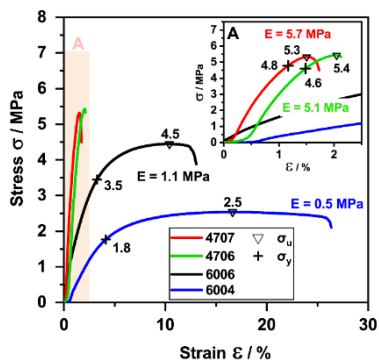
Figure 3.8 Stress-strain diagram of the green tapes; the elastic modulus, yield and ultimate stresses are indicated.

Optical photographs in Figure 3.9 show the defectless flat structure of the tape 6006 with its good handling and rolling capability.
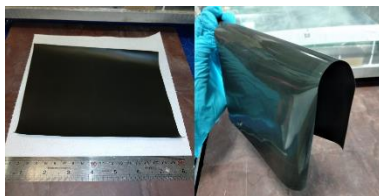
Figure 3.9 Optical photographs of the tape 6006

3.5   Homogeneity and Consistency

Maintaining tape homogeneity and consistency during the tape casting process is one of the fundamental issues in the industrial use of water as a solvent, which makes it demanding to obtain a consistent thickness as well. The homogeneity of green tape is largely dependent on the rearrangement of starting particles during sintering which is heavily dependent on solid packing in the green tape [139]. From the statistical point of view, if a tape's weight, in-plane dimension, and thickness

alternate proportionately across the tape during sintering, it is anticipated that the relative standard deviation (RSD), also known as the error (standard deviation (SD)) to mean ratio, will be equal for these alternations. Owing to this proportionality, the tape can be regarded as homogenous. A polygon will be obtained by plotting RSD on a radar chart. The closer the centroid of this polygon to the zero point of the plot, the more equal are RSDs and thus, the more homogeneous the tape. If RSDs are smaller as well, all the better. Since the tape benefits both from a good homogeneity and a high consistency as well.

Figure 3.10 illustrates a comparative radar chart of RSD for weight, in-plane, and thickness changes in tapes after sintering. The data were gathered from the center, edges, beginning, and end of each tape in eight samples as seen in Table 3.1. Every tape displayed a significant RSD for thickness shrinkage. Table 3.2 shows detailed values of these RSD and the centroid to zero distance. As solid loading and viscosity decreased, this got worse. For 60 wt% solid loading tapes, the polygonal centroid is closer to zero, indicating that the tape's weight, in-plane dimensions, and thickness all altered proportionally. As a result, the 60 wt% solid loading tapes are more homogenous. To be clear, the hydrostatic pressure changes during casting or the shear stress of the moving blade had the least impact on the slurry's composition. High solid loading has a noticeable impact on achieving homogenous tapes. Smaller particle spacing and less solvent aid in producing a more even distribution of particles. The most homogeneity was seen in tape 6006, with the most equal RSD.
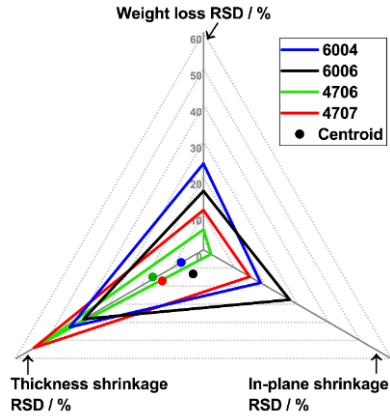
Figure 3.10 Tapes homogeneity based on measured RSD for weight, in-plane, and thickness alternations after sintering.

Table 3.1 Thickness shrinkage, in-plane shrinkage and weight loss measurements in different spots of the tapes

	R-value (wt%)		Sample nr.	Weight Loss (g)	In-plane Shrinkage (mm)	Thickness Shrinkage (μm)
6004	1.27		1	0.0733	3.46	55
			2	0.0702	5.28	90
			3	0.0848	3.80	60
			4	0.0794	3.20	41
			5	0.0866	3.93	43
			6	0.0470	4.22	113
			7	0.0560	4.20	38
			8	0.0465	5.26	95
		Mean		0.06798	4.16820	66.875
		SD		0.01621	0.76183	28.5729
		RSD		23.84043	18.2771	42.72583
6006	1.09		1	0.0584	2.33	110
			2	0.0742	4.10	49
			3	0.0645	4.07	30
			4	0.0656	3.96	87
			5	0.0611	1.93	60
			6	0.0540	3.87	80

		7	0.0410	3.94	116
		8	0.0638	2.45	96
		Mean	0.06033	3.33388	78.5
		SD	0.00977	0.92018	30.10458
		RSD	16.18888	27.60083	38.34978
4706	0.84	1	0.0484	4.23	19
		2	0.0452	3.97	60
		3	0.0511	4.04	20
		4	0.0451	4.02	50
		5	0.0510	3.98	70
		6	0.0496	4.10	33
		7	0.0523	4.13	90
		8	0.0475	4.20	77
		Mean	0.04877	4.08375	52.375
		SD	0.00271	0.09782	26.54881
		RSD	5.56187	2.39546	50.68985
4707	0.56	1	0.0546	4.45	27
		2	0.0503	2.50	50
		3	0.0521	3.94	84
		4	0.0504	4.05	40
		5	0.0561	3.90	84
		6	0.039	3.79	20
		7	0.0499	3.93	34
		8	0.0448	3.92	30
		Mean	0.04965	3.81016	46.125
		SD	0.00548	0.56499	25.00536
		RSD	11.0343	14.82856	54.21216

Table 3.2 RSD measurements in tapes with different R-value

	R-value (wt%)	RSD Weight Loss	RSD In-plane Shrinkage	RSD Thickness Shrinkage	RSD Error	Centroid to Zero Distance (Point)
6004	1.27	23.8	18.3	42.7	±12.8	9.1
6006	1.09	16.2	27.6	38.3	±11.0	7.7
4706	0.84	5.6	2.4	50.7	±27.0	22.8
4707	0.56	11.0	14.8	54.2	± 23.9	15.8

3.6   Plasticizer to Binder Ratio Effect on Sintering

3.6.1   Density and Porosity

After sintering, the maximum relative density of 95.5% is achieved for tape 6006 in terms of theoretical density (d = 6.321 g cm^{-3}), as shown in Figure 3.11, which was validated by Archimedes' density analysis. Thus, it has the lowest closed porosity. The proportion of closed porosity increases as open-pore channels are more pinched off. This leads to reduced density at 47 wt% (17.0 vol.%) of solid loading as well as less water absorption. For tapes 6004, 6006, 4706, and 4707, the water absorption as a percentage of sample mass is calculated to be 8.4, 7.0, 5.9, and 6.2 wt%, respectively.
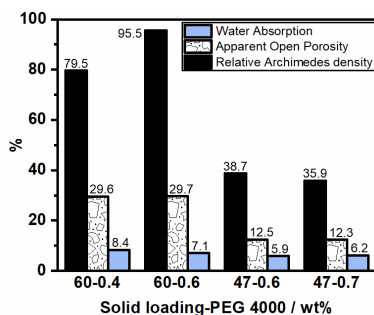
Figure 3.11 Apparent density, porosity, and water absorption of sintered tapes

3.6.2   Microstructure

All sintered tapes show similar mesoporous structures following the heat treatment at 1200 °C. However, among other tapes, tape 6006 shows fainter grain boundaries, more rounded edges, and densification that is greater than grain growth. Figure 3.12 shows the FESEM images of the tapes' 4706 and 6006 surfaces, after sintering at 1200 °C.
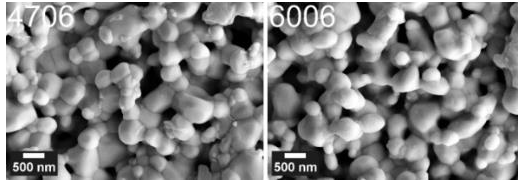
Figure 3.12 FESEM images of tapes 4706 and 6006 surfaces sintered at 1200 °C

3.6.3 Anisotropicity

Figures 3.13a and b, respectively, depict dilatometric shrinkages in longitudinal and perpendicular to casting directions with varying R-values. different R-values. Tapes with 47 wt% (17.0 vol.) solid loading show lower longitudinal shrinkages but larger perpendicular one than the tapes 60 wt% (18.5 vol.%) solid loading. The cross-section SEM images after sintering are shown in Figure 3.13c. Significantly, larger pore anisotropy is observed at 47 wt% (17.0 vol.%) solid loading, with large $K_{(L,P)}$ = 21.6%–29.4%. At low solid loading, the polymeric matrix is more dominant in controlling the anisotropic shrinkage. The elongation of PEG 4000 polymers beneath the moving blade during casting results in elongated pores after sintering, as shown by larger shrinkage in the perpendicular direction. When the solid loading is increased to 60 wt% (18.5 vol.%), polymer elongation is balanced in both directions, and this makes the shrinkage to be more isotropic and brings about lower $K_{(L,P)}$ = 4.0% for 6004 and −1.4% for 6006. Regardless of the sign, the lowest value was achieved for tape 6006. Thus, it is reasonable to conclude that at R-value = 0.84 wt%, Duramax B1000 and PEG 4000 polymers form a uniform network where the solid particles are oriented in both directions to the same extent, resulting in a similar shrinkage percentage in both directions.
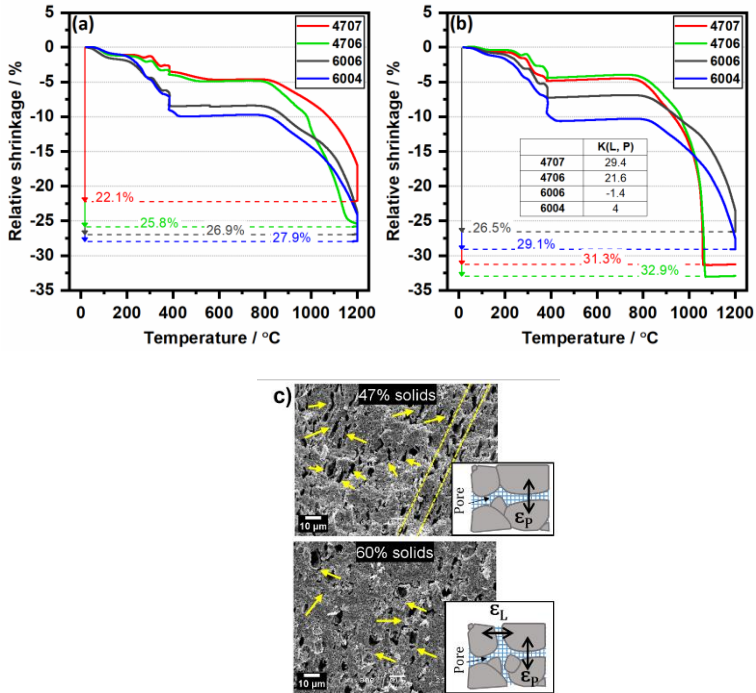
Figure 3.13 Dilatometric shrinkage in a) longitudinal, and b) perpendicular direction to casting. The calculated anisotropic factor $K_{(L, P)}$ is also shown. c) Pore anisotropy in tapes of 47 wt% and 60 wt% solid loading

3.7 Plasticizer to Binder Ratio Effect on Redox Stability

3.7.1 Reducing

To determine the sintered tapes' stability under redox conditions, they were subjected to reduction and oxidation cycles. Figure 3.14 shows the XRD patterns recorded on the tapes after the reduction step. LSCF mainly decomposes to R.P. oxides, largely $(La_{0.38}Sr_{0.62})_2FeO_4$ and La_2CoO_4. During reduction, the change in the oxidation state of Fe^{4+} and Co^{4+} makes their exsolution easier towards the surface, which

leads to the formation of CoFe alloy nanoparticles. Lanthanum oxide (La_2O_3) is also formed as secondary phase.
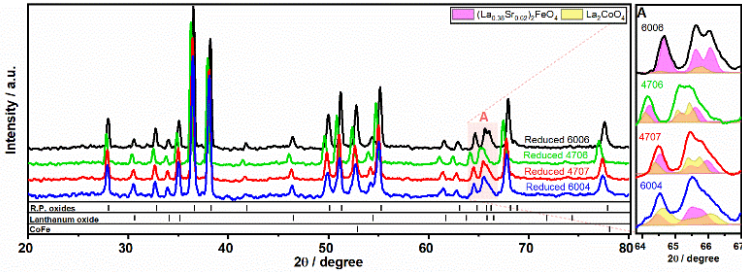
Figure 3.14 XRD pattern of sintered tapes after the reduction (H_2/Ar) step for 10 h at 900 °C. Inset (A): cobalt oxide to ferrite peaks

Table 3.2 shows the reduction quantitative analysis results, performed by the Rietveld refinement. In all tapes, less amount of new cobaltite was seen than ferrite, except in tape 6004, with the most amount of La_2CoO_4 (38.9 wt%). However, the smallest amount of La_2CoO_4 was achieved for tape 6006 (9.2 wt%). Inset A in Figure 3.14 shows a double peak at $2\theta \approx 66°$ derived from both R.P. oxides. The yellow phase shows cobalt oxide, and the pink phase is related to ferrite. Moving from 6004 to 6006, the double peak gets sharper and more splitted as the contribution of ferrite increases. Tape 6004 shows the broadest peaks while the tape 6006 shows the sharpest pattern.

This alternation trend is followed on surface morphology as well, after reduction. This is confirmed by the FESEM image analysis shown in Figure 3.15. A study by Park et al. [59] revealed that the bulky support phase is related to R.P. oxides which on their surface, CoFe nanoparticles are exsolved. The tapes 6004 and 4707 with higher amounts of La_2CoO_4 (Table 3.3) shows a bulkier support phase, due to a larger unit cell volume of La_2CoO_4 (V = 378 Å^3) than $(La_{0.38}Sr_{0.62})_2FeO_4$ (V = 189 Å^3). The semi-sphere shape of CoFe nanoparticles (25–50 nm) implies that they are utterly socketed on the surface. Owing to the minimized energy barriers for nucleation of Co at grain boundaries, reduced Co ions are exsolved from the bulk and

diffuse towards the grain boundaries to form nucleation centres together with Fe [140]. Thus, CoFe agglomerations are observed along the grain boundaries. The tape 6006 maintains its microstructure to the maximum extent after reduction, owing to more amount of iron R.P. oxide and the proximity of its unit cell volume to the one for LSCF (V = 350 Å^3).
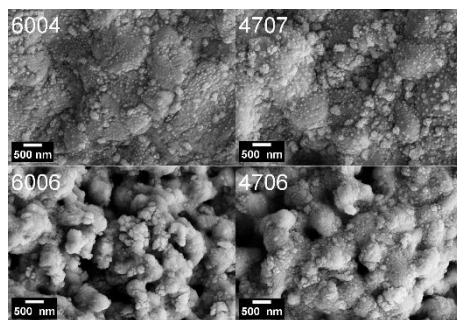
Figure 3.15 FESEM images of sintered tapes subjected to reducing conditions

Table 3.3 Phase weight fractions (wt%) after reducing cycle

	6004	6006	4706	4707	Error
(La0.38Sr0.62)2FeO4	34.8	64.2	49.6	42.5	±1.5
La2CoO4	38.9	9.2	23.5	28.4	±1.8
La2O3	9.8	8.5	10.4	10.0	±0.4
CoFe	16.4	18.0	16.5	19.2	±0.7

3.7.2 Oxidizing

The tapes are substantially stable when subjected to the oxidative cycle in pure air at 900 °C for 10 h. No trace of any newly formed phase or degradation is observed. A little peak shifting is observed. An assumption is that the further stress inside the LSCF lattice is likely to be relieved by partial strontium migration to the surface, to minimize the surface charge and segregate as strontium oxides and hydroxide (≈ 1 wt%) [141], [142]. Thus, the Sr migration rate might be affected by the available surface area and porosity of the samples. Figure 3.16

shows XRD patterns recorded on sintered tapes after the oxidation step. Inset B shows that the peaks are more shifted towards higher angles in two tapes 6006 and 4706, concerning the peaks in Inset A. This indicates different changes in LSCF unit cell volume; probably, due to different amounts of Sr migration.
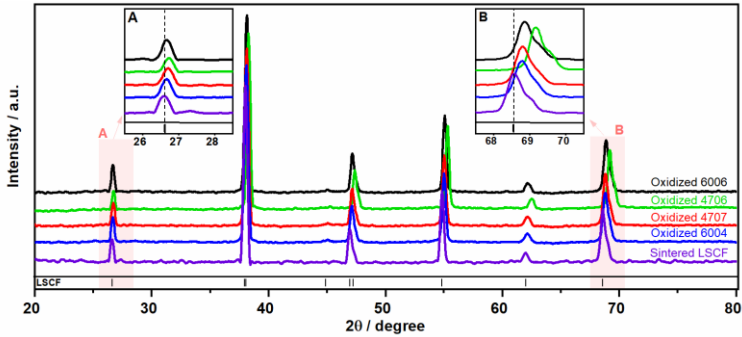
Figure 3.16 XRD pattern of sintered tapes after the oxidation step for 10 h at 900°C. Peak shifting is compared in two insets (A) and (B)

III.   STEP 3: SOFC Characterization

3.8   LSCFMo Anodic Stability

XRD analysis was used to investigate the influence of Mo^{6+} doping and partial replacement for Fe^{4+} on the phase and microstructural stability of LSCF, as shown in Figure 3.17. After the reduction, LSCF was entirely dissolved into R.P. oxides and CoFe alloy nanoparticles. The phase stability was improved by increasing the Mo dopant concentration. LSCFMo5 dissolved into R.P. oxides and CoFe nanoparticles but it retained some of its perovskite rhombohedral structure. This is in contrast with respect to LSCFMo10, which demonstrated excellent phase stability after reduction and could be retained up to 60 wt% with just a small quantity of newly produced R.P. oxides. After sintering and reduction, the peak intensity for $SrMoO_4$ decreased significantly. The reason is assumed to be due to reduction of Mo^{6+} to Mo^{5+} which partially enters into the LSCF structure [71].
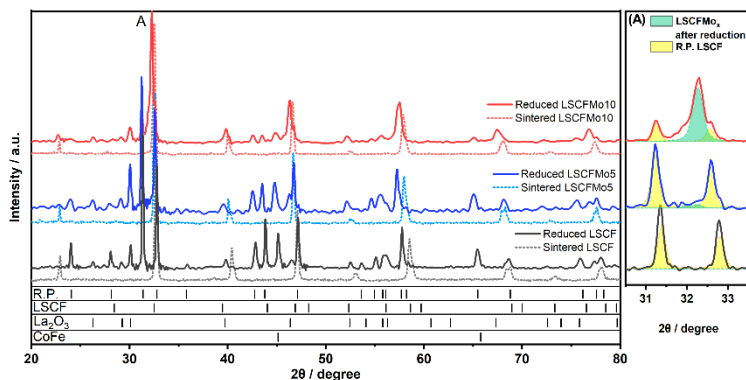
Figure 3.17 XRD pattern of LSCF, LSCFMo5 and LSCFMo10 after reduction in Ar/H_2 at 900°C for 10 h

The peak ratio between the residual perovskite (green in Fig. 3.17) and the newly created R.P. oxides (yellow) after reduction is shown in the inset (A) of Figure 3.17. By increasing the Mo dopant, this ratio increases. It is thought that under low partial oxygen pressures, an ion

with large radius, such as Mo^{6+} in the B-site, can accommodate Sr^{3+} in the A-site, suppressing Sr activation and dissolution [68]. Furthermore, Mo^{6+} can moderate further reduction of Fe^{3+}/Fe^{2+} into the metallic phase, this preventing the collapse of the perovskite structure. This is because the redox bands of mixed-valent Mo^{5+}/Mo^{6+} and Fe^{3+}/Fe^{2+} couples overlap [65], which has been proved by XPS investigations in another study [66]. The main peak for LSCFMo is shifted before and after reduction thus pointing out a variation of the unit cell volume and parameters induced by the heat treatment but not corresponding to some kind of decomposition.

Figure 3.18 shows the SEM images taken from the surface of as-sintered and reduced LSCFMo tapes. Along with the results from XRD, the tape LSCFMo10 shows the most retained microstructure and porosity following reduction. The LSCFMo5 tape shows a larger grain size and higher (about 30%) bulk density after reduction. Due to the complete decomposition of LSCF after reduction and the larger cell volume of R.P. oxides with respect to LSCF, the bulk density is increased by about 70%.
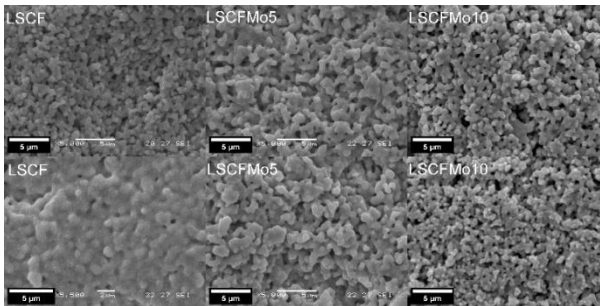
Figure 3.18 SEM images from the surface of sintered (top) and reduced (bottom) LSCFMo$_x$ tapes

3.9 Cell Macro/Micro-Structure

After co-sintering, integrated and flattened button-SOFC with good mechanical properties were obtained. Mo5 and Mo10 will now

refer to cells with anodes made of LSCFMo5 and LSCFMo10, respectively.
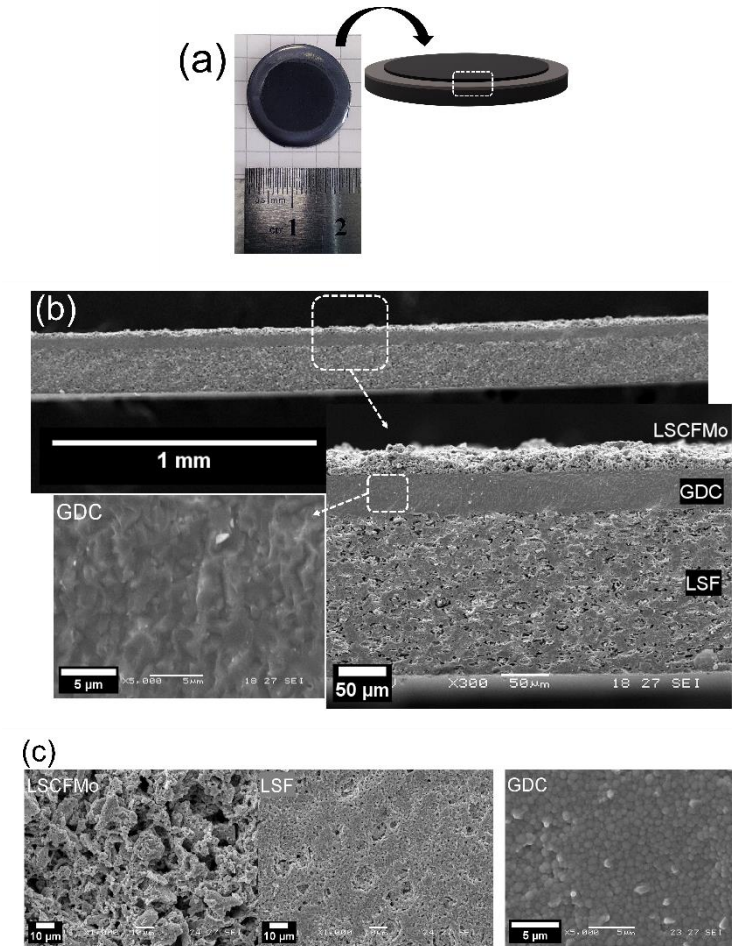
Figure 3.19 a) Photograph and 3D schematic of a co-sintered button-cell; SEM images of b) cell cross-section, c) anode, cathode and electrolyte surface after co-sintering (this latter correspond to non-coated regions on the border of the cell).

Figure 3.19 shows the final cell design and structure. The cross-section microstructure of the cells after co-sintering is shown in Figure 3.19a. The cell consists of LSCFMo porous anode, thick GDC electrolyte and LSF cathode. The thickness of the LSF cell's support layer is 170 µm; the thickness of the GDC electrolyte is 40 µm. While LSF and GDC benefit from a uniform thickness as a result of the tape casting process, LSCFMo anode thickness varies in the range of 20–35 µm after repeated screen-printing. Both the anode and cathode are well-attached to the GDC electrolyte and no delamination is observed throughout the entire cell. Lu et al. [70] and Zhang et al. [72] found that Mo doping into $Pr_{0.6}Sr_{0.4}(Fe_{0.8}Ni_{0.2})_{1-x}Mo_xO_{3-\delta}$ and $Pr_{0.4}Sr_{0.6}(Co_{0.2}Fe_{0.8})_{1-x}Mo_xO_{3-\delta}$, respectively, decreased the TEC significantly as Mo dopant was increased. The presence of a high-valent element like Mo in the structure can suppress the reduction of B-site cations (Fe^{4+}, Co^{3+}, Ni^{4+}) to their lower valence states (Fe^{3+}, Co^{2+}, Ni^{3+}) and thus, the TEC is decreasing. As a result, the compatibility between electrode and electrolyte is increased, delaying cracking and failure in the cell during heating or redox cycles. The surface microstructure of LSCFMo, LSF and GDC is shown in Figure 3.19b. After co-sintering, a total porosity of 36% for the anode and 15% for the cathode was determined, these being adequate for fuel and oxygen availability at triple phase boundaries (TPBs). A dense GDC layer is achieved with only some isolated and small pores. The cross-section SEM image of GDC shows almost merged grains, yet when the surface is examined, grain boundaries can be detected (Figure 3.19c).

3.10   Electrochemical Performance

3.10.1 OCV and Durability

Figure 3.20a shows OCV measurements. During the pre-treatment of the anode with He gas at 600 °C, a very low OCV (0.04 V) is recorded. When the cell is supplied with biogas (30 cm³/min CH_4 + 20 cm³/min CO_2), the potential increases to 0.05 V, which is still lower than the practical potential. The cells were then supplied with pure dry methane at the following stages. The potential is only marginally

enhanced, reaching 0.06 V, as a result of the higher partial pressure of CH_4. Despite the fact that the potential is steadily independent of fuel type, the low OCV shows that LSCFMo has extremely weak electrocatalytic activity and acts as an inert for direct methane oxidation.

To investigate the best biofuel and catalytic mechanism for LSCFMo, the cell was fed methanol (0.5 cm³/ h CH_3OH + 25 cm³/ min He) at 600 °C. Figure 3.20b shows the OCV measurements. Surprisingly, the cell potential quickly increases. In LSCFMo, which works with biofuels other than biogas and methane, the "shuttle mechanism" is the main mechanism. Lo Faro et al. [143] proposed the shuttle mechanism to occur when dry alcohol fuels are used with lanthanum ferrites. Lanthanum ferrites are not powerful enough as anodic catalysts to perform direct oxidation of biofuels, while methanol is oxidized through several subsequent processes. "Shuttle mechanism" begins with the dehydrogenation of methanol and then, the oxidation of CO and H_2 residues (Figure 3.20c) [23]. It is suggested that the methanol dehydrogenation and cracking-free reactions are promoted by molybdenum dopant in LSCF, and the reactions are given by

$$CH_3OH \xrightarrow{LSCFMo} -CH_2O_{(ads)} + H_2 \quad Dehydrogenation \quad (3.4)$$

$$H_2 + O^{2-} \xrightarrow{LSCFMo} H_2O + 2e^- \qquad Oxidation \qquad (3.5)$$

$$-CH_2O_{(ads)} + H_2O \xrightarrow{LSCFMo} 2H_2 + CO_2 \qquad (3.6)$$

$$CO_2 + H_2 \xrightarrow{LSCFMo} CO + H_2O \qquad (3.7)$$

$$CO + O^{2-} \xrightarrow{LSCFMo} CO_2 + 2e^- \qquad Oxidation \qquad (3.8)$$
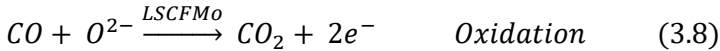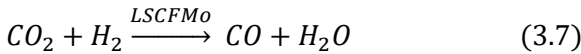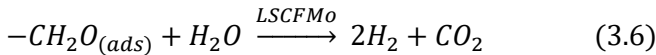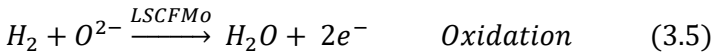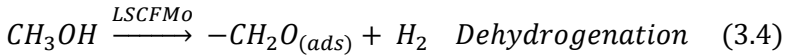
Although LSCFMo shows good catalytic activity towards methanol oxidation, the potential is low, probably because GDC10 becomes partially electronically conductive. The overall voltage loss

after 1.5 h, on the other hand, could be reduced by adjusting the fuel flow settings.
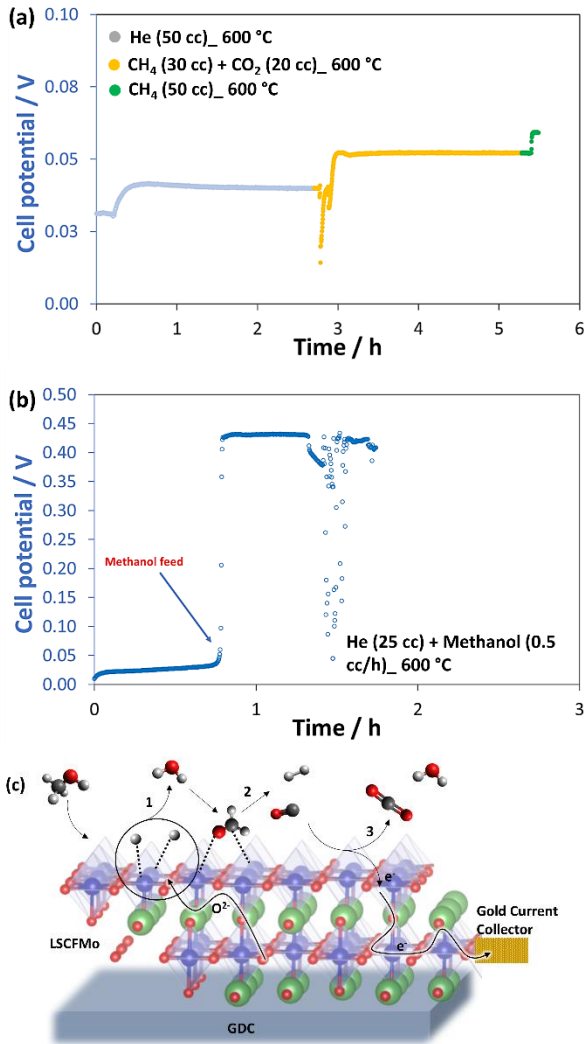
Figure 3.20 OCV measurements at 600°C of the cells fed by a) He, biogas, and pure methane and b) He and methanol. c) Suggested schematic of "shuttle mechanism" in methanol oxidation on Mo-doped LSCF

Figure 3.21 shows the short-time durability tests of the cells Mo5 and Mo10 while being fed by different fuels at 600 °C and 700 °C. In line with previous OCV studies, a very low potential is recorded at open circuit current when the cells are fed by biogas and methane. The potential is boosted to 0.55 V after feeding the cell Mo5 with methanol at 600 °C, although the performance diminishes rapidly after 5 h. This value is just slightly lower than the average OCV for SOFC with GDC10 electrolyte (around 0.60 V [60]). One can see in Figure 3.21b that increasing the temperature to 700 °C does not make a big difference in OCV, although the performance degrades slower. The performance becomes stable when the cell is fed by hydrogen. With H_2 at 700 °C, an OCV of 0.74 V is recorded, and the potential drops down to 0.20 V when the current is loaded. Nevertheless, the performance is stable for almost 4 h. Figure 3.21c shows that Mo10 behaves similarly to Mo5 at 600 °C. Feeding Mo10 with methanol, the achieved OCV is 0.47 V but with a rapid decline after loading current. Because He may trigger the removal of methanol fuel from the anode's active sites, less He was injected into the flow. As a result, the performance deterioration rate is minimized. The deterioration rate may be improved by adjusting the flow rate and fuel ratio. After that, the cell was fed by pure H_2 for about 7 h. Although the OCV is a bit lower than Mo5, it is assumed to be related to earlier defects developed in the cell Mo10 during the tests. Another reason might be related to the presence of very low amounts of $SrMoO_4$, as this secondary phase is non-conductive and can limit the electroconductivity and OCV [144]. Nevertheless, this OCV shows a certain reactivity of LSCFMo towards hydrogen and methanol oxidation although it is gradually lost.
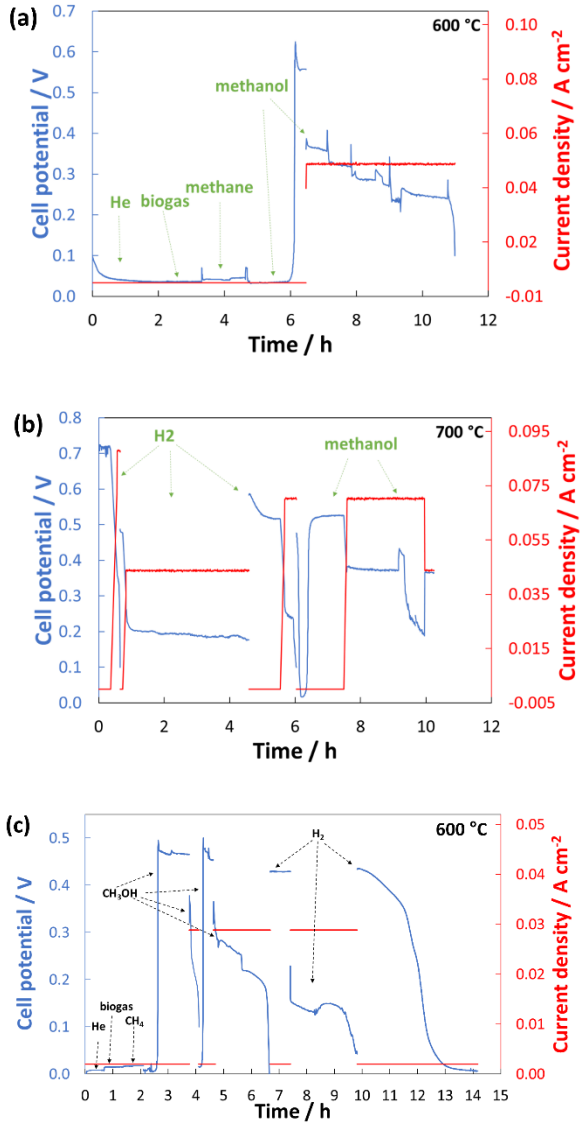
Figure 3.21 Short-term durability of cells a) Mo5 at 600 °C, b) Mo5 at 700 °C and c) Mo10 at 600 °C

3.10.2 EIS

Each EIS spectrum contains information concerning the series resistance (R_S), which is primarily caused by the ionic resistance of the electrolyte, and RQ elements in series, which are ascribable to cell reaction resistances. Figure 3.22 shows the impedance spectra for different fuels at 600 °C. Figure 3.22a shows three RQ elements for both Mo5 and Mo10 cells when fed by biogas and methane. The large semicircles imply a significant kinetic barrier to direct methane oxidation. A smaller semicircle at high frequencies indicates the low activation control on the cathode side. It is porous enough and air can easily access TPBs. However, the larger semicircles at medium and low frequencies are taken as the poor electrocatalytic activity of LSCFMo towards the direct methane oxidation and related oxidation intermediates. Nevertheless, R_S is approximately 0.20 Ω cm^2 and does not vary significantly with the type of fuel which is seen as a positive aspect.

Figures 3.22b and 3.22c show the EIS spectra from the cells Mo5 and Mo10, respectively, fed by methanol. The series resistance is as low as 0.14 Ω cm^2 in Mo10 which indicates the good innovative configuration and design of the cell. At least two RQ elements are visible in both cells, with additional semicircles in Mo10. The first and second RQ are related to the dehydrogenation of methanol, and CO and H$_2$ oxidations on the anode side, respectively. It was previously confirmed that LSCFMo10 preserves the perovskite structure under reducing conditions, while LSCFMo5 is more decomposed to R.P. oxides. Figure 3.22d shows LSCFMo and its R.P. oxide structure. Higher reduction stability in LSCFMo10 can protect the bond bridge Fe^{3+}–O–Fe^{4+} in the structure which prevents further increase in the activation energy of electron transfer [59], [75]. Whereas, in LSCFMo5, more activation energy is required to transfer the electron due to the gap between layers. As a result, the first semicircle which is affected by the activation control of anodic reactions is smaller in Mo10 than in Mo5. A similar result in enhancing charge transfer by Mo doping into lanthanum ferrites was proved by Hou et al. [75], who showed that higher reduction stability can also bring about an increase in electroconductivity of Mo-doped La$_{0.6}$Sr$_{0.4}$Fe$_{0.9}$Ni$_{0.1}$O$_{3-\delta}$, at a wide

temperature range (500–850 °C). The additional RQ elements in Mo10 are related to O_2 reduction on the cathode side and the adsorption and dissociation of dry organic molecules which gets facilitated as the He carrier arises. The total polarization resistance is larger in cell Mo5 than in Mo10.
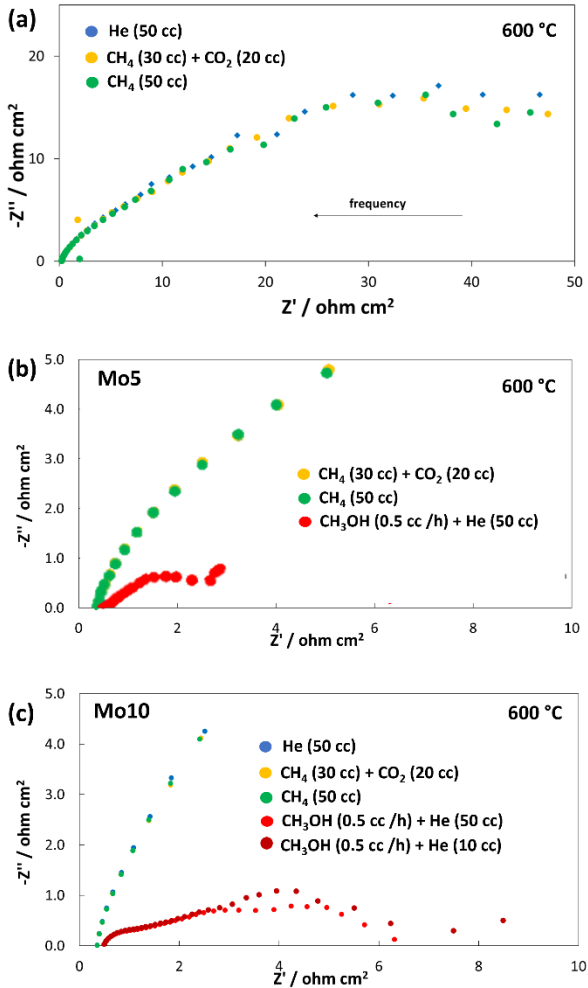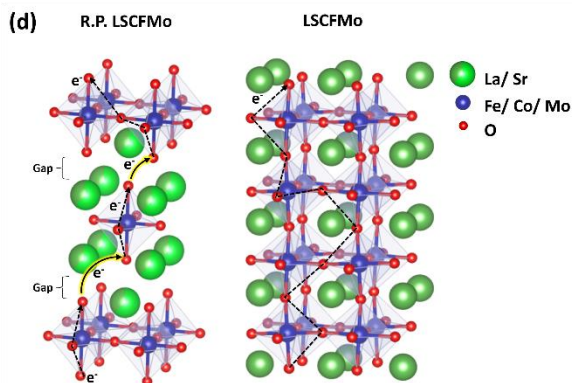
Figure 3.22 EIS plots of the cells at 600°C when fed by a) H_2, biogas and methane, b) methanol in cell Mo5, and c) methanol in cell Mo10. d) Charge transfer in LSCFMo and its R.P. oxide

3.10.3 I-V Curves

Figure 3.23 compares the polarization curves of the various tested cells. The fast drop in voltage, around 200 mV, indicates an increase in activation control in both cells towards methanol oxidation, due to overvoltage after loading the current. By increasing the operating temperature to 700 °C (Figure 3.23b), the activation control perfectly disappears, and the maximum power density is almost doubled. This is because at a higher temperature, charge transfer is facilitated, and electrochemical activity increases. However, due to low OCV, the maximum power density reaches 32 and 38 mW cm^{-2} for methanol and hydrogen fuel, respectively. The practical issue with SOFC while being fed by alcohol fuels is usually their low maximum power density (MPD) owing to higher anodic activation loss [145]. There are studies on alcohol-fueled SOFC that delivered very low MPD (<100 mW cm^{-2}) even with noble metal-based anodes [146]. Furthermore, although Mo-based perovskites are commonly used as anode in SOFCs (due to their high redox stability and good carbon tolerance), their MPD is sometimes low even at 800 °C [48]. Similar $La_{0.5}Sr_{0.5}Fe_{0.9}Mo_{0.1}O_{3-d}$ and $Pr_{0.6}Sr_{0.4}Fe_{0.7}Ni_{0.2}Mo_{0.1}O_{3-\delta}$ delivered

MPD of 190 mW cm^{-2} [147] and 162 mW cm^{-2} [148], respectively, at 650 °C in H$_2$. In other studies, Sr$_2$TiNi$_{0.5}$Mo$_{0.5}$O$_6$ and La$_{0.3}$Sr$_{0.7}$Ti$_{0.97}$Mo$_{0.03}$O$_{3-d}$ delivered MPD of ~100 mW cm^{-2} (at 700 °C) [78] and 60 mW cm^{-2} (at 800 °C) [71] in H$_2$, respectively. Nevertheless, MPD is always affected not just by the anode composition, but also by TPB and microstructure of the anode and can be limited by OCV. Here, considering the low operating temperature of 600 °C and the dry methanol feed, besides the low achieved OCV, the cell delivered MPD of ~35 mW cm^{-2}. The hypothesis is that either the LSCFMo composition or the electrode microstructure must be optimized to achieve faster electrocatalytic activity and higher power density. Still, LSCFMo is a promising anode material in SOFCs to process the oxidation of methanol with no carbon deposition. In cell Mo10, a similar behavior to Mo5 is observed at 600 °C (Figure 3.23c). The performances were improved by decreasing the methanol dilution, although the injection of He as carrier is necessary.
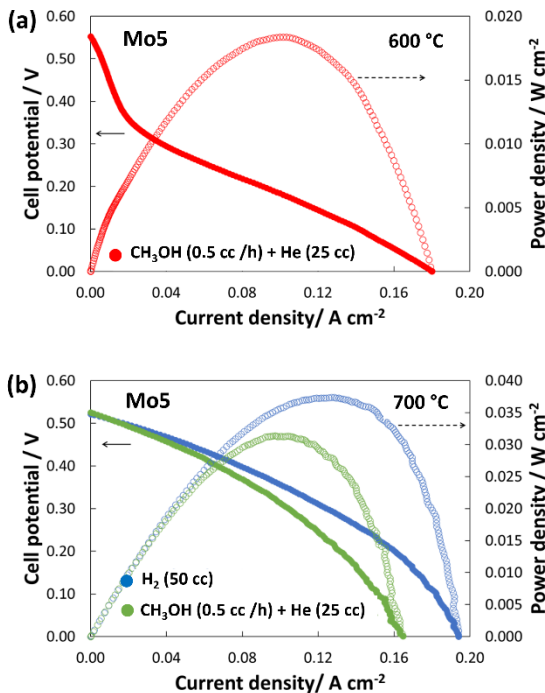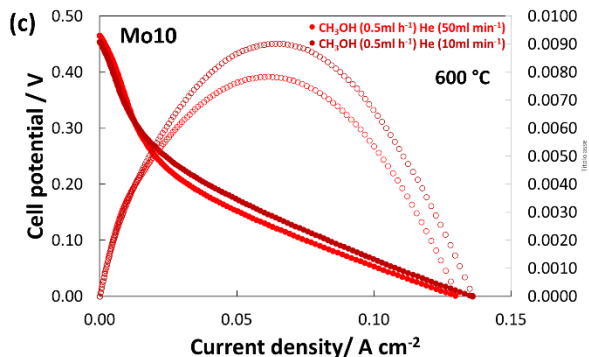
Figure 3.23 Polarization curves for the cells a, b) Mo5 at 600 °C and 700 °C, and c) Mo10 at 600 °C

3.10.4 Carbon Deposition

Interestingly, after the tests, no trace of any carbon was found on the anode side nor in the anodic tube although all the fuels were dry. Any cracking is excluded from the shuttle mechanism which is a positive result and is accompanied by no carbon deposition at the end. However, there is a high possibility of Boudouard or water-gas reverse reactions occurrence at low temperatures, given respectively by

$$2CO \leftrightarrow CO_2 + C \qquad \Delta H^{\circ}_{298} = -171 \; kJ/mol \qquad (3.9)$$

$$H_2 + CO \leftrightarrow H_2O + C \qquad \Delta H^{\circ}_{298} = -131 \; kJ/mol \qquad (3.10)$$
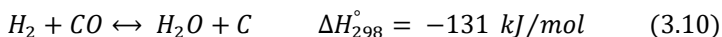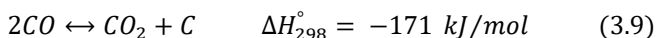
However, as previously mentioned (see chapter 1, section 1.8), under reducing conditions, Mo^{6+} is reduced to Mo^{5+} which brings about more oxygen vacancies just around the active B-site cations like Mo^{6+}. Therefore, the instant formation and consumption of activated carbon species increases the tolerance of the anode towards carbon adsorption in the structure. Also, it was mentioned that the higher structural stability induced by Mo doping prevents further metal cluster formations on the surface which hampers enough surface provide for carbon deposition.

Conclusion

For an LT/IT-SOFC to work efficiently and with more delayed performance degradation, the cell design and materials are required to be designed carefully. Here, a molybdenum-doped LSCF was designed and synthesized as the anodic alternative material and a water-based tape casting procedure was developed to fabricate thick cathodes as the support layers of the SOFC, using PEG 4000 as a high M_W plasticizer instead of common low M_W ones.

Regarding the cathode design, by adjusting the R-value at 0.84 wt% of PEG 4000 (plasticizer) to Duramax B1000 (binder) during the slurry preparation and setting the relative humidity at RH = 70% during the drying, thick green cathode layers with E = 1.1 MPa were fabricated. The tapes could be rolled down to a minimum bending radius of 2.57 mm and benefitted from a high mechanical strength up to σ_u = 4.5 MPa. This could bring about lower residual stresses during further lamination and can also promise a continuous casting and rolling of tapes in industrial massive production. Another important issue was to maintain the thickness constant during casting which could result in higher homogeneity over the same tapes. The least anisotropicity and the highest density up to 95.5%, after sintering could be achieved when the R-value was adjusted to 0.84 wt%.

As a result, the R-value = 0.84 wt% and RH = 70% could be proposed as promising composition and processing parameters for a reliable water-based tape casting of lanthanum ferrite cathode layers in industrial scale, that are suitable for further lamination or co-sintering processes.

Talking about the anodic material, Mo was doped successfully into LSCF by the auto-combustion method. An increased phase and microstructural stability were observed under reducing conditions by increasing the Mo dopant and substituting for Fe and Co in LSCF. XRD analysis proved that LSCFMo10 retained the initial perovskite structure up to 60 wt% under reducing conditions in H_2 at 900 °C. Electrochemical measurements showed that biogas and methane are

the least reactive fuels. Whereas LSCFMo is capable of oxidizing methanol through a "shuttle mechanism". Since the first reaction is the dehydrogenation of methanol and it needs less activation energy with respect to methane direct oxidation, the perovskite follows this mechanism as proved by OCV and EIS. The very low series resistance proved a very good configuration of the realized cells. A 10% Mo dopant showed slightly better catalytic activity towards methanol oxidation than 5% Mo, and no trace of carbon deposition was found on the anode side after feeding the cells with dry biofuels. The chemical stability of LSCFMo is preserved after the electrochemical tests. Molybdenum's redox gap overlapping with B-site cations, lower TEC, and quick surface exchange make it a suitable choice as a dopant in LSCF. As a result, the LSCFMo anode may be offered as an active electrocatalyst in IT-SOFCs for methanol oxidation.

As a result, this project could successfully innovate an IT-SOFC by tape casting as a colloidal process, and co-sintering, that can be fed by methanol as a biofuel. It is proved that LSCFMo can be used as an alternative to the anode material. No carbon deposition was detected after the tests. The cell integrity and mechanical strength are preserved during the tests.

Future Perspectives

To realize effective commercialized SOFCs that can operate above 40,000 h and to use them practically in industry, novel technologies or transport systems, huge gaps need to be filled. Regarding the LT-SOFC in this project, many options exist which can be considered to improve the cell potential or prolong its lifetime. Some more important and specific aspects are as follows:

I.   To improve the cell potential, the GDC electrolyte layer needs to be modified. The dopant Gd amount can be optimized for an optimized sealing.

II.   To improve the catalytic activity and to make the cell fuel flexible, the anode perovskite formulation can be modified and adjusted based on the final reduced structure of the perovskite.

Activities

Conferences & Seminars

- 25th European Fuel Cell Forum Conference (EFCF 2021) - Low-Temperature Electrolysers, Fuel Cells, and H2 Processing [29 Jun- 2 Jul 2021] (Lucerne, Switzerland)
- 15th EFCF forum, SOFC & SOE Forum [5-8 Jul. 2022] (Lucerne, Switzerland)
- Ceramics in Europe conference [9-14 Jul. 2022] (Krakow, Poland)
- PhD DII poster session [13 May 2022] (Trento, Italy)
- 30 years of INSTM Convegno [22-25 Jan. 2023] (Bressanone, Italy)

Schools

- Online summer School on "Electric and Magnetic Field-assisted Processing of Inorganic Materials" [14-16 Sep. 2020]
- European School on Ceramics for Energy Conversion and Storage (EnergyCeram) [25-27 Nov. 2020]
- Renewable energies, Energy storage and Hydrogen economy [23-27 Aug. 2021] (Udine, Italy)

Workshops

- Workshop on "Women of distinction in materials science"
- Electron Microscopy Perspectives

Publications

1. Alemayehu A, Biesuz M, Javan KY, *et al.* Ultrafast high-temperature sintering of gadolinia-doped ceria. *J Eur Ceram Soc*. 2023;43(11):4837–4843. https://doi.org/10.1016/j.jeurceramsoc.2023.04.025

2. Javan KY, Sglavo VM. Influence of drying conditions and plasticizer-to-binder ratio on the water-based tape casting of La0.6Sr0.4Co0.2Fe0.8O3−δ. *Int J Appl Ceram Technol*. 2024. https://doi.org/10.1111/IJAC.14691

3. Javan KY, Lo Faro M, Vecino-Mantilla S, Sglavo VM. Mo-Doped LSCF as a Novel Coke-Resistant Anode for Biofuel-Fed SOFC. *Materials (Basel)*. 2024;17(4). https://doi.org/10.3390/ma17040869

References

[1]   P. J. Megia, A. J. Vizcaino, J. A. Calles, and A. Carrero, "Hydrogen Production Technologies: From Fossil Fuels toward Renewable Sources. A Mini Review," *Energy and Fuels*, vol. 35, no. 20, pp. 16403–16415, Oct. 2021, doi: 10.1021/ACS.ENERGYFUELS.1C02501/ASSET/IMAGES/LARGE/EF1C02501_0004.JPEG.

[2]   P. Pablo-Romero *et al.*, "A Global Assessment: Can Renewable Energy Replace Fossil Fuels by 2050?," *Sustain. 2022, Vol. 14, Page 4792*, vol. 14, no. 8, p. 4792, Apr. 2022, doi: 10.3390/SU14084792.

[3]   V. Zepf, *The dependency of renewable energy technologies on critical resources*. Elsevier Inc., 2020. doi: 10.1016/B978-0-12-819534-5.00004-0.

[4]   V. Quaschning, *Understanding Renewable Energy Systems*, 2nd ed. Taylor & Francis, 2016. [Online]. Available: https://books.google.it/books?id=zSveCwAAQBAJ

[5]   T. Z. Ang, M. Salem, M. Kamarol, H. S. Das, M. A. Nazari, and N. Prabaharan, "A comprehensive study of renewable energy sources: Classifications, challenges and suggestions," *Energy Strateg. Rev.*, vol. 43, p. 100939, Sep. 2022, doi: 10.1016/J.ESR.2022.100939.

[6]   M. Vujanović, Q. Wang, M. Mohsen, N. Duić, and J. Yan, "Special issue of applied energy dedicated to SDEWES conferences 2018: Sustainable energy technologies and environmental impacts of energy systems," *Appl. Energy*, vol. 256, no. September, 2019, doi: 10.1016/j.apenergy.2019.113919.

[7]   F. Barbir, "Transition to renewable energy systems with hydrogen as an energy carrier," *Energy*, vol. 34, no. 3, pp. 308–312, 2009, doi: 10.1016/j.energy.2008.07.007.

[8]   S. KELOUWANI, K. AGBOSSOU, and R. CHAHINE, "Model for energy conversion in renewable energy system with hydrogen storage," *J. Power Sources*, vol. 140, no. 2, pp. 392–399, Feb. 2005, doi: 10.1016/j.jpowsour.2004.08.019.

[9]   Y. Kalinci, A. Hepbasli, and I. Dincer, "Biomass-based hydrogen production: A review and analysis," *Int. J. Hydrogen Energy*, vol. 34, no. 21, pp. 8799–8817, 2009, doi: 10.1016/j.ijhydene.2009.08.078.

[10]   C. Breyer *et al.*, "On the History and Future of 100% Renewable Energy Systems Research," *IEEE Access*, vol. 10, pp. 78176–78218, 2022, doi: 10.1109/ACCESS.2022.3193402.

[11]   P. Moriarty and D. Honnery, "Feasibility of a 100% Global Renewable Energy System," *Energies 2020, Vol. 13, Page 5543*, vol. 13, no. 21, p. 5543, Oct. 2020, doi: 10.3390/EN13215543.

[12]   N. A. Baharuddin, N. F. Abdul Rahman, H. Abd. Rahman, M. R. Somalu, M. A. Azmi, and J. Raharjo, "Fabrication of high-quality electrode films for solid oxide fuel cell by screen printing: A review on important processing parameters," *Int. J. Energy Res.*, vol. 44, no. 11, pp. 8296–8313, Sep. 2020, doi: 10.1002/ER.5518.

[13]   T. Emil and H. Preis, "Uber brennstoff-ketten mit festleitern.," no. 0.

[14]   S. C. Singhal, "Solid oxide fuel cells for power generation," *WIREs Energy Environ.*, vol. 3, no. 2, pp. 179–194, 2014, doi: 10.1002/wene.96.

[15]   Z. Gao, L. V. Mogni, E. C. Miller, J. G. Railsback, and S. A. Barnett, "A perspective on low-temperature solid oxide fuel cells," *Energy Environ. Sci.*, vol. 9, no. 5, pp. 1602–1644, 2016, doi: 10.1039/c5ee03858h.

[16]   J. Patakangas, Y. Ma, Y. Jing, and P. Lund, "Review and analysis of characterization methods and ionic conductivities for low-temperature solid oxide fuel cells (LT-SOFC)," *J. Power Sources*, vol. 263, pp. 315–331, Oct. 2014, doi: 10.1016/J.JPOWSOUR.2014.04.008.

[17]   V. De Marco, A. Grazioli, and V. M. Sglavo, "Production of planar copper-based anode supported intermediate temperature solid oxide fuel cells cosintered at 950 °C," *J. Power Sources*, vol. 328, pp. 235–240, 2016, doi: https://doi.org/10.1016/j.jpowsour.2016.08.025.

[18]   C. Mendonça, A. Ferreira, and D. M. F. Santos, "Towards the

Commercialization of Solid Oxide Fuel Cells: Recent Advances in Materials and Integration Strategies," *Fuels 2021, Vol. 2, Pages 393-419*, vol. 2, no. 4, pp. 393–419, Oct. 2021, doi: 10.3390/FUELS2040023.

[19] R. Vinoth Kumar and A. P. Khandale, "A review on recent progress and selection of cobalt-based cathode materials for low temperature-solid oxide fuel cells," *Renew. Sustain. Energy Rev.*, vol. 156, p. 111985, Mar. 2022, doi: 10.1016/J.RSER.2021.111985.

[20] N. S. Mohd Affandi and N. Osman, "Short review on global trends in SOFC scenario and future perspective," *Mater. Today Proc.*, vol. 66, no. P10, pp. 3981–3984, 2022, doi: 10.1016/j.matpr.2022.04.824.

[21] M. J. B. Kabeyi and O. A. Olanrewaju, "Biogas Production and Applications in the Sustainable Energy Transition," *J. Energy*, vol. 2022, pp. 1–43, Jul. 2022, doi: 10.1155/2022/8750221.

[22] L. A. Silva, A. R. Martins, A. Ballarini, S. Maina, and M. do C. Rangel, "Evaluation of nickel and copper catalysts in biogas reforming for hydrogen production in SOFC," *Matéria (Rio Janeiro)*, vol. 22, no. 1, 2017, doi: 10.1590/s1517-707620170001.0134.

[23] M. Lo Faro, V. Antonucci, P. L. Antonucci, and A. S. Aricò, "Fuel flexibility: A key challenge for SOFC technology," *fuel*, vol. 102, pp. 554–559, 2012, doi: https://doi.org/10.1016/j.fuel.2012.07.031.

[24] S. A. Saadabadi, A. Thallam Thattai, L. Fan, R. E. F. Lindeboom, H. Spanjers, and P. V. Aravind, "Solid Oxide Fuel Cells fuelled with biogas: Potential and constraints," *Renew. Energy*, vol. 134, pp. 194–214, Apr. 2019, doi: 10.1016/J.RENENE.2018.11.028.

[25] M. F. Vostakola and B. A. Horri, "Progress in Material Development for Low-Temperature Solid Oxide Fuel Cells: A Review," *Energies 2021, Vol. 14, Page 1280*, vol. 14, no. 5, p. 1280, Feb. 2021, doi: 10.3390/EN14051280.

[26] G. Chasta, | Himanshu, | Mahendra, S. Dhaka, and M. Singh Dhaka, "A review on materials, advantages, and challenges in thin film based solid oxide fuel cells," *Int. J. Energy Res.*, vol. 46, no. 11, pp. 14627–14658, Sep. 2022, doi: 10.1002/ER.8238.

[27]   C. Liu, J. Pu, X. Chen, Z. Ma, and X. Ding, "ScienceDirect Influence of anode ' s microstructure on electrochemical performance of solid oxide direct carbon fuel cells," *Int. J. Hydrogen Energy*, vol. 45, no. 20, pp. 11784–11790, 2020, doi: 10.1016/j.ijhydene.2020.02.119.

[28]   Z. Zakaria, Z. Awang Mat, S. H. Abu Hassan, and Y. Boon Kar, "A review of solid oxide fuel cell component fabrication methods toward lowering temperature," *Int. J. Energy Res.*, vol. 44, no. 2, pp. 594–611, 2020, doi: 10.1002/er.4907.

[29]   M. Bilal Hanif *et al.*, "Recent advancements, doping strategies and the future perspective of perovskite-based solid oxide fuel cells for energy conversion," *Chem. Eng. J.*, vol. 428, no. August 2021, 2022, doi: 10.1016/j.cej.2021.132603.

[30]   S. A. Muhammed Ali *et al.*, "Carbonate-based lanthanum strontium cobalt ferrite (LSCF)-samarium-doped ceria (SDC) composite cathode for low-temperature solid oxide fuel cells," *Appl. Sci.*, vol. 10, no. 11, p. 3761, Jun. 2020, doi: 10.3390/app10113761.

[31]   W.-J. Yin, B. Weng, J. Ge, Q. Sun, Z. Li, and Y. Yan, "Oxide perovskites, double perovskites and derivatives for electrocatalysis, photocatalysis, and photovoltaics," *Energy Environ. Sci.*, vol. 12, no. 2, pp. 442–462, 2019, doi: 10.1039/C8EE01574K.

[32]   R. Jacobs, T. Mayeshiba, J. Booske, and D. Morgan, "Material Discovery and Design Principles for Stable, High Activity Perovskite Cathodes for Solid Oxide Fuel Cells," *Adv. Energy Mater.*, vol. 8, no. 11, p. 1702708, 2018, doi: 10.1002/aenm.201702708.

[33]   S. P. Jiang, "Development of lanthanum strontium cobalt ferrite perovskite electrodes of solid oxide fuel cells – A review," *Int. J. Hydrogen Energy*, vol. 44, no. 14, pp. 7448–7493, Mar. 2019, doi: 10.1016/J.IJHYDENE.2019.01.212.

[34]   F. Zurlo, A. Iannaci, V. M. Sglavo, and E. Di Bartolomeo, "Copper-based electrodes for IT-SOFC," *J. Eur. Ceram. Soc.*, vol. 39, no. 1, pp. 17–20, Jan. 2019, doi: 10.1016/j.jeurceramsoc.2018.02.029.

[35]   S. Onbilgin, B. Timurkutluk, C. Timurkutluk, and S. Celik, "Comparison of electrolyte fabrication techniques on the performance of anode supported solid oxide fuel cells," *Int. J.*

Hydrogen Energy, 2020, doi: https://doi.org/10.1016/j.ijhydene.2020.01.097.

[36]   P. Vinchhi, M. Khandla, K. Chaudhary, and R. Pati, "Recent advances on electrolyte materials for SOFC: A review," *Inorg. Chem. Commun.*, vol. 152, no. April, p. 110724, 2023, doi: 10.1016/j.inoche.2023.110724.

[37]   M. Choolaei, M. F. Vostakola, and B. A. Horri, "Recent Advances and Challenges in Thin-Film Fabrication Techniques for Low-Temperature Solid Oxide Fuel Cells," *Cryst. 2023, Vol. 13, Page 1008*, vol. 13, no. 7, p. 1008, Jun. 2023, doi: 10.3390/CRYST13071008.

[38]   F. Wang, Y. Lyu, D. Chu, Z. Jin, G. Zhang, and D. Wang, "The electrolyte materials for SOFCs of low-intermediate temperature: review," *Mater. Sci. Technol.*, vol. 35, no. 13, pp. 1551–1562, Sep. 2019, doi: 10.1080/02670836.2019.1639008.

[39]   G. Xiao and F. Chen, "Redox stable anodes for solid oxide fuel cells," *Front. Energy Res.*, vol. 2, no. JUN, p. 99291, Jun. 2014, doi: 10.3389/FENRG.2014.00018/BIBTEX.

[40]   S. Vafaeenezhad, A. R. Hanifi, M. A. Laguna-Bercero, T. H. Etsell, and P. Sarkar, "Microstructure and long-Term stability of Ni-YSZ anode supported fuel cells: A review," *Mater. Futur.*, vol. 1, no. 4, 2022, doi: 10.1088/2752-5724/ac88e7.

[41]   H. Su and Y. H. Hu, "Progress in low-temperature solid oxide fuel cells with hydrocarbon fuels," *Chem. Eng. J.*, vol. 402, p. 126235, Dec. 2020, doi: 10.1016/J.CEJ.2020.126235.

[42]   M. Rafique, H. Nawaz, M. Shahid Rafique, M. Bilal Tahir, G. Nabi, and N. R. Khalid, "Material and method selection for efficient solid oxide fuel cell anode: Recent advancements and reviews," *Int. J. Energy Res.*, vol. 43, no. 7, pp. 2423–2446, Jun. 2019, doi: 10.1002/ER.4210.

[43]   S. Tao and J. T. S. Irvine, "A redox-stable efficient anode for solid-oxide fuel cells," *Nature Materials*, vol. 2, no. 5. European Association for Cardio-Thoracic Surgery, pp. 320–323, Mar. 30, 2003. doi: 10.1038/nmat871.

[44]   Z. Tao, M. Fu, and Y. Liu, "A mini-review of carbon-resistant

anode materials for solid oxide fuel cells," *Sustain. Energy Fuels*, vol. 5, no. 21, pp. 5420–5430, 2021, doi: 10.1039/d1se01300a.

[45]   N. Shi *et al.*, "Review of anodic reactions in hydrocarbon fueled solid oxide fuel cells and strategies to improve anode performance and stability," *Mater. Renew. Sustain. Energy*, vol. 9, no. 1, p. 6, 2020, doi: 10.1007/s40243-020-0166-8.

[46]   P. Boldrin, E. Ruiz-Trejo, J. Mermelstein, J. M. Bermúdez Menéndez, T. Ramírez Reina, and N. P. Brandon, "Strategies for Carbon and Sulfur Tolerant Solid Oxide Fuel Cell Materials, Incorporating Lessons from Heterogeneous Catalysis," *Chem. Rev.*, vol. 116, no. 22, pp. 13633–13684, 2016, doi: 10.1021/acs.chemrev.6b00284.

[47]   A. P. E. York, T. C. Xiao, M. L. H. Green, and J. B. Claridge, "Methane Oxyforming for Synthesis Gas Production," *Catal. Rev.*, vol. 49, no. 4, pp. 511–560, Oct. 2007, doi: 10.1080/01614940701583315.

[48]   A. N. Zainon *et al.*, "Challenges in using perovskite-based anode materials for solid oxide fuel cells with various fuels: a review," *Int. J. Hydrogen Energy*, vol. 48, no. 53, pp. 20441–20464, 2023, doi: 10.1016/j.ijhydene.2022.12.192.

[49]   L. Shu, J. Sunarso, S. S. Hashim, J. Mao, W. Zhou, and F. Liang, "Advanced perovskite anodes for solid oxide fuel cells: A review," *Int. J. Hydrogen Energy*, vol. 44, no. 59, pp. 31275–31304, Nov. 2019, doi: 10.1016/J.IJHYDENE.2019.09.220.

[50]   Y. Hu, J. Li, and S. Wang, "Evaluation of oxygen vacancy and carbon deposition effect at the perovskite on methane adsorption," *Comput. Mater. Sci.*, vol. 219, no. December 2022, 2023, doi: 10.1016/j.commatsci.2023.112020.

[51]   M. Li, B. Hua, J. Pu, B. Chi, and L. Jian, "Electrochemical performance and carbon deposition resistance of M-BaZr0.1Ce0.7Y0.1Yb0.1O3-δ (M = Pd, Cu, Ni or NiCu) anodes for solid oxide fuel cells," *Sci. Reports 2015 51*, vol. 5, no. 1, pp. 1–7, Jan. 2015, doi: 10.1038/srep07667.

[52]   D. Montinaro, M. Bertoldi, and V. M. Sglavo, "Synthesis and Processing of Perovskite Oxides for Solid Oxide Fuel Cells Anode Fabrication," *Adv. Sci. Technol.*, vol. 45, pp. 1864–1868, Oct. 2006,

doi: 10.4028/www.scientific.net/ast.45.1864.

[53]   P. R. Slater, D. P. Fagg, and J. T. S. Irvine, "Synthesis and electrical characterisation of doped perovskite titanates as potential anode materials for solid oxide fuel cells," *J. Mater. Chem.*, vol. 7, no. 12, pp. 2495–2498, 1997, doi: 10.1039/A702865B.

[54]   B. Kayaalp *et al.*, "Surface Reconstruction under the Exposure of Electric Fields Enhances the Reactivity of Donor-Doped SrTiO3," *J. Phys. Chem. C*, vol. 123, no. 27, pp. 16883–16892, Jul. 2019, doi: 10.1021/ACS.JPCC.9B04620/ASSET/IMAGES/LARGE/JP-2019-04620Q_0004.JPEG.

[55]   C. C. Chen, M. M. Nasrallah, and H. U. Anderson, "Preparation and Electrode Characteristics of Dense La0.6Sr0.4Co0.2Fe0.8O3 Thin Film by Polymeric Precursors," *ECS Proc. Vol.*, vol. 1993–4, no. 1, p. 252, Jan. 1993, doi: 10.1149/199304.0252PV.

[56]   C. C. Chen, M. M. Nasrallah, and H. U. Anderson, "Cathode/Electrolyte Interactions and Their Expected Impact On SOFC Performance," *ECS Proc. Vol.*, vol. 1993–4, no. 1, p. 598, Jan. 1993, doi: 10.1149/199304.0598PV.

[57]   S. Li, W. Jin, N. Xu, and J. Shi, "Synthesis and oxygen permeation properties of La0.2Sr0.8Co0.2Fe0.8O3-δ membranes," *Solid State Ionics*, vol. 124, no. 1, pp. 161–170, Sep. 1999, doi: 10.1016/S0167-2738(99)00136-8.

[58]   H. Chang, H. Chen, Z. Shao, J. Shi, J. Bai, and S.-D. Li, "In situ fabrication of (Sr,La)FeO4 with CoFe alloy nanoparticles as an independent catalyst layer for direct methane-based solid oxide fuel cells with a nickel cermet anode," *J. Mater. Chem. A*, vol. 4, no. 36, pp. 13997–14007, 2016, doi: 10.1039/C6TA04639H.

[59]   S. Park, H. Han, J. Choi, S. Lee, M. Park, and W. B. Kim, "Ruddlesden–Popper Oxide (La0.6Sr0.4)2(Co,Fe)O4 with Exsolved CoFe Nanoparticles for a Solid Oxide Fuel Cell Anode Catalyst," *Energy Technol.*, vol. 9, no. 7, Jul. 2021, doi: 10.1002/ENTE.202100116.

[60]   M. Lo Faro, S. C. Zignani, and A. S. Aricò, "Lanthanum Ferrites-Based Exsolved Perovskites as Fuel-Flexible Anode for Solid Oxide Fuel Cells," *Mater. 2020, Vol. 13, Page 3231*, vol. 13, no. 14, p. 3231, Jul. 2020, doi: 10.3390/MA13143231.

[61]   A. J. Fernández-Ropero, J. M. Porras-Vázquez, A. Cabeza, P. R. Slater, D. Marrero-López, and E. R. Losilla, "High valence transition metal doped strontium ferrites for electrode materials in symmetrical SOFCs," *J. Power Sources*, vol. 249, pp. 405–413, Mar. 2014, doi: 10.1016/J.JPOWSOUR.2013.10.118.

[62]   Y. Shen *et al.*, "Mo-doped Ba0.5Sr0.5Co0.8Fe0.2O3-δ as a high-performance symmetric electrode for solid oxide fuel cells," *J. Alloys Compd.*, vol. 928, p. 167029, Dec. 2022, doi: 10.1016/J.JALLCOM.2022.167029.

[63]   X. Yang *et al.*, "Improving stability and electrochemical performance of Ba0.5Sr0.5Co0.2Fe0.8O3-δ electrode for symmetrical solid oxide fuel cells by Mo doping," *J. Alloys Compd.*, vol. 831, p. 154711, Aug. 2020, doi: 10.1016/j.jallcom.2020.154711.

[64]   L. Bian *et al.*, "Highly stable La0.5Sr0.5Fe0.9Mo0.1O3-δ electrode for reversible symmetric solid oxide cells," *Int. J. Hydrogen Energy*, vol. 45, no. 38, pp. 19813–19822, Jul. 2020, doi: 10.1016/J.IJHYDENE.2020.05.117.

[65]   J. B. Goodenough and Y. H. Huang, "Alternative anode materials for solid oxide fuel cells," *J. Power Sources*, vol. 173, no. 1, pp. 1–10, Nov. 2007, doi: 10.1016/J.JPOWSOUR.2007.08.011.

[66]   Z. Du *et al.*, "High-Performance Anode Material Sr2FeMo0.65Ni0.35O6 - δ with in Situ Exsolved Nanoparticle Catalyst," *ACS Nano*, vol. 10, no. 9, pp. 8660–8669, 2016, doi: 10.1021/acsnano.6b03979.

[67]   Y. Liu, F. Zhou, X. Chen, C. Wang, and S. Zhong, "Enhanced electrochemical activity and stability of LSCF cathodes by Mo doping for intermediate temperature solid oxide fuel cells," *J. Appl. Electrochem.*, vol. 51, no. 3, pp. 425–433, Mar. 2021, doi: 10.1007/S10800-020-01515-Z/TABLES/3.

[68]   D. M. Neacsa *et al.*, "Nb and Cu co-doped (La,Sr)(Co,Fe)O 3 : a stable electrode for solid oxide cells," *RSC Adv.*, vol. 11, no. 18, pp. 10479–10488, Mar. 2021, doi: 10.1039/D0RA10313F.

[69]   S. Wang *et al.*, "Mo-doped La0·6Sr0·4FeO3-δ as an efficient fuel electrode for direct electrolysis of CO2 in solid oxide electrolysis cells," *Electrochim. Acta*, vol. 337, p. 135794, 2020, doi:

https://doi.org/10.1016/j.electacta.2020.135794.

[70] X. Lu *et al.*, "Mo-doped Pr0.6Sr0.4Fe0.8Ni0.2O3-δ as potential electrodes for intermediate-temperature symmetrical solid oxide fuel cells," *Electrochim. Acta*, vol. 227, pp. 33–40, 2017, doi: https://doi.org/10.1016/j.electacta.2016.12.170.

[71] J. Li *et al.*, "Molybdenum substitution at the B-site of lanthanum strontium titanate anodes for solid oxide fuel cells," *Int. J. Hydrogen Energy*, vol. 42, no. 34, pp. 22294–22301, 2017, doi: 10.1016/j.ijhydene.2017.03.189.

[72] P. Zhang *et al.*, "B-site Mo-doped perovskite Pr0.4Sr0.6 (Co0.2Fe0.8)1−xMoxO3−σ (x = 0, 0.05, 0.1 and 0.2) as electrode for symmetrical solid oxide fuel cell," *J. Power Sources*, vol. 276, pp. 347–356, 2015, doi: https://doi.org/10.1016/j.jpowsour.2014.11.141.

[73] Z. Xie, H. Zhao, Z. Du, T. Chen, and N. Chen, "Electrical, chemical, and electrochemical properties of double perovskite oxides Sr2Mg1- xNixMoO6-δ as anode materials for solid oxide fuel cells," *J. Phys. Chem. C*, vol. 118, no. 33, pp. 18853–18860, 2014, doi: 10.1021/jp502503e.

[74] A. Aguadero, D. Pérez-Coll, J. A. Alonso, S. J. Skinner, and J. Kilner, "A New Family of Mo-Doped SrCoO3−δ Perovskites for Application in Reversible Solid State Electrochemical Cells," *Chem. Mater.*, vol. 24, no. 14, pp. 2655–2663, 2012, doi: 10.1021/cm300255r.

[75] Y. Hou, L. Wang, L. Bian, N. Chen, and K. Chou, "High performance of Mo-doped La0.6Sr0.4Fe0.9Ni0.1O3-δ perovskites as anode for solid oxide fuel cells," *Electrochim. Acta*, vol. 292, pp. 540–545, 2018, doi: https://doi.org/10.1016/j.electacta.2018.09.190.

[76] G. Amow, I. J. Davidson, and S. J. Skinner, "A comparative study of the Ruddlesden-Popper series, Lan+1NinO3n+1 (n = 1, 2 and 3), for solid-oxide fuel-cell cathode applications," *Solid State Ionics*, vol. 177, no. 13–14, pp. 1205–1210, 2006, doi: 10.1016/j.ssi.2006.05.005.

[77] Y. S. Chung *et al.*, "In situ preparation of a La1.2Sr0.8Mn0.4Fe0.6O4 Ruddlesden-Popper phase with exsolved Fe nanoparticles as an anode for SOFCs," *J. Mater. Chem. A*, vol. 5,

no. 14, pp. 6437–6446, 2017, doi: 10.1039/c6ta09692a.

[78]   B. He, Z. Wang, L. Zhao, X. Pan, X. Wu, and C. Xia, "Ti-doped molybdenum-based perovskites as anodes for solid oxide fuel cells," *J. Power Sources*, vol. 241, pp. 627–633, 2013, doi: https://doi.org/10.1016/j.jpowsour.2013.04.148.

[79]   H. Li, Y. Tian, Z. Wang, F. Qie, and Y. Li, "An all perovskite direct methanol solid oxide fuel cell with high resistance to carbon formation at the anode," *RSC Adv.*, vol. 2, no. 9, pp. 3857–3863, 2012, doi: 10.1039/c2ra01256a.

[80]   R. Moreno, "Better ceramics through colloid chemistry," *J. Eur. Ceram. Soc.*, vol. 40, no. 3, pp. 559–587, Mar. 2020, doi: 10.1016/J.JEURCERAMSOC.2019.10.014.

[81]   D. Zou, M. Qiu, X. Chen, E. Drioli, and Y. Fan, "One step co-sintering process for low-cost fly ash based ceramic microfiltration membrane in oil-in-water emulsion treatment," *Sep. Purif. Technol.*, vol. 210, pp. 511–520, Feb. 2019, doi: 10.1016/j.seppur.2018.08.040.

[82]   V. M. Sglavo and N. Bellettati, "Ceramic laminates with improved mechanical reliability by tailoring the porosity of the constituting layers," *J. Eur. Ceram. Soc.*, vol. 37, no. 4, pp. 1643–1650, Apr. 2017, doi: 10.1016/J.JEURCERAMSOC.2016.11.022.

[83]   V. M. Sglavo and M. Bertoldi, "Design and production of ceramic laminates with high mechanical reliability," *Compos. Part B Eng.*, vol. 37, no. 6, pp. 481–489, Jan. 2006, doi: 10.1016/J.COMPOSITESB.2006.02.001.

[84]   V. M. Sglavo, M. Paternoster, and M. Bertoldi, "Tailored Residual Stresses in High Reliability Alumina-Mullite Ceramic Laminates," *J. Am. Ceram. Soc.*, vol. 88, no. 10, pp. 2826–2832, Oct. 2005, doi: 10.1111/J.1551-2916.2005.00479.X.

[85]   M. Cologna, V. M. Sglavo, and M. Bertoldi, "Sintering and Deformation of Solid Oxide Fuel Cells Produced by Sequential Tape Casting," *Int. J. Appl. Ceram. Technol.*, vol. 7, no. 6, pp. 803–813, 2010, doi: 10.1111/j.1744-7402.2009.02390.x.

[86]   J. H. Myung, H. J. Ko, C. H. Im, J. Moon, and S. H. Hyun, "Development of solid oxide fuel cells (SOFCs) by tape-casting and

single-step co-firing of monolithic laminates," *Int. J. Hydrogen Energy*, vol. 39, no. 5, pp. 2313–2319, Feb. 2014, doi: 10.1016/J.IJHYDENE.2013.11.122.

[87]   R. Mistler, "Tape Casting: Theory and Practice - Richard E. Mistler, Eric R. Twiname - Google Libri." https://books.google.it/books/about/Tape_Casting.html?id=boF5Qg AACAAJ&redir_esc=y (accessed Jun. 15, 2021).

[88]   "Effects of Suspension Composition on Defects in Aqueous Tape Casting of Alumina Ceramics: A Rheological Study," *Journal of the Korean Ceramic Society*, vol. 42, no. 1. pp. 1–6, 2005. doi: 10.4191/kcers.2005.42.1.001.

[89]   D. Hotza and P. Greil, "Review: aqueous tape casting of ceramic powders," *Mater. Sci. Eng. A*, vol. 202, no. 1–2, pp. 206–217, Nov. 1995, doi: 10.1016/0921-5093(95)09785-6.

[90]   W. Schafbauer *et al.*, "Tape casting as a multi purpose shaping technology for different applications in energy issues," *Mater. Sci. Forum*, vol. 706–709, pp. 1035–1040, 2012, doi: 10.4028/www.scientific.net/MSF.706-709.1035.

[91]   D. Montinaro *et al.*, "Tape casting fabrication and co-sintering of solid oxide 'half cells' with a cathode–electrolyte porous interface," *Solid State Ionics*, vol. 177, no. 19–25, pp. 2093–2097, Oct. 2006, doi: 10.1016/J.SSI.2006.01.016.

[92]   S. Iliescu and J. Situ, "Water-Based Tape Casting Process : An Environmentally Friendly Process for Mass Production of Ceramic Substrates for Electronic Applications *," vol. 9, pp. 30–32, 2021.

[93]   S. Ann Jose, K. K.A., and S. Kuzhichalil Peethambharan, "Aqueous tape casting of Al2O3-BBSZ based LTCC multilayer substrates," *Mater. Res. Bull.*, vol. 140, p. 111289, Aug. 2021, doi: 10.1016/J.MATERRESBULL.2021.111289.

[94]   L. Wang, G. Tang, and Z. K. Xu, "Comparison of water-based and solvent-based tape casting for preparing multilayer ZnO varistors," *J. Am. Ceram. Soc.*, vol. 91, no. 11, pp. 3742–3745, Nov. 2008, doi: 10.1111/j.1551-2916.2008.02677.x.

[95]   J. Luo and R. Eitel, "Aqueous tape casting of Al2O3 for multilayer co-fired ceramic based microfluidic chips with translucent

windows," *Ceram. Int.*, vol. 44, no. 3, pp. 3488–3491, Feb. 2018, doi: 10.1016/J.CERAMINT.2017.11.076.

[96]   J. Nie, M. Li, W. Liu, W. Li, and Z. Xing, "The role of plasticizer in optimizing the rheological behavior of ceramic pastes intended for stereolithography-based additive manufacturing," *J. Eur. Ceram. Soc.*, vol. 41, no. 1, pp. 646–654, Jan. 2021, doi: 10.1016/J.JEURCERAMSOC.2020.08.013.

[97]   S. Foghmoes, F. Teocoli, K. Brodersen, T. Klemensø, and M. Della Negra, "Novel ceramic processing method for substitution of toxic plasticizers," *J. Eur. Ceram. Soc.*, vol. 36, no. 14, pp. 3441–3449, Nov. 2016, doi: 10.1016/J.JEURCERAMSOC.2016.05.043.

[98]   D. H. Kim, K. Y. Lim, U. Paik, and Y. G. Jung, "Effects of chemical structure and molecular weight of plasticizer on physical properties of green tape in BaTiO3/PVB system," *J. Eur. Ceram. Soc.*, vol. 24, no. 5, pp. 733–738, 2004, doi: 10.1016/S0955-2219(03)00256-5.

[99]   M. Rahman and C. S. Brazel, "The plasticizer market: an assessment of traditional plasticizers and research trends to meet new challenges," *Prog. Polym. Sci.*, vol. 29, no. 12, pp. 1223–1248, Dec. 2004, doi: 10.1016/J.PROGPOLYMSCI.2004.10.001.

[100]   K. Sungkajuntranon, P. Sribenjalux, S. Supothina, and P. Chuaybamroong, "Effect of binders on airborne microorganism inactivation using TiO2 photocatalytic fluorescent lamps," *J. Photochem. Photobiol. B Biol.*, vol. 138, pp. 160–171, Sep. 2014, doi: 10.1016/J.JPHOTOBIOL.2014.05.019.

[101]   F. Laboulfie, M. Hémati, A. Lamure, and S. Diguet, "Effect of the plasticizer on permeability, mechanical resistance and thermal behaviour of composite coating films," *Powder Technol.*, vol. 238, pp. 14–19, Apr. 2013, doi: 10.1016/J.POWTEC.2012.07.035.

[102]   M. Jabbari, R. Bulatova, A. I. Y. Tok, C. R. H. Bahl, E. Mitsoulis, and J. H. Hattel, "Ceramic tape casting: A review of current methods and trends with emphasis on rheological behaviour and flow analysis," *Mater. Sci. Eng. B*, vol. 212, pp. 39–61, Oct. 2016, doi: 10.1016/J.MSEB.2016.07.011.

[103]   H. J. Kim, M. J. M. Krane, K. P. Trumble, and K. J. Bowman, "Analytical fluid flow models for tape casting," *J. Am. Ceram. Soc.*,

vol. 89, no. 9, pp. 2769–2775, Sep. 2006, doi: 10.1111/J.1551-2916.2006.01163.X.

[104]   A. Heunisch, A. Dellert, and A. Roosen, "Effect of powder, binder and process parameters on anisotropic shrinkage in tape cast ceramic products," *J. Eur. Ceram. Soc.*, vol. 30, no. 16, pp. 3397–3406, Dec. 2010, doi: 10.1016/J.JEURCERAMSOC.2010.08.012.

[105]   F. A. Houle, R. E. H. Miles, C. J. Pollak, and J. P. Reid, "A purely kinetic description of the evaporation of water droplets," *J. Chem. Phys.*, vol. 154, no. 5, p. 054501, Feb. 2021, doi: 10.1063/5.0037967.

[106]   B. J. Briscoe, G. Lo Biundo, and N. Özkan, "Drying kinetics of water-based ceramic suspensions for tape casting," *Ceram. Int.*, vol. 24, no. 5, pp. 347–357, Jan. 1998, doi: 10.1016/S0272-8842(97)00021-7.

[107]   G. W. Scherer, "Theory of Drying," *J. Am. Ceram. Soc.*, vol. 73, no. 1, pp. 3–14, 1990, doi: 10.1111/j.1151-2916.1990.tb05082.x.

[108]   M. Jabbari, V. A. Jambhekar, J. H. Hattel, and R. Helmig, "Drying of a tape-cast layer: Numerical modelling of the evaporation process in a graded/layered material," *Int. J. Heat Mass Transf.*, vol. 103, pp. 1144–1154, Dec. 2016, doi: 10.1016/J.IJHEATMASSTRANSFER.2016.08.073.

[109]   R. Evans, "The interpretation of small molecule diffusion coefficients: Quantitative use of diffusion-ordered NMR spectroscopy," *Prog. Nucl. Magn. Reson. Spectrosc.*, vol. 117, pp. 33–69, Apr. 2020, doi: 10.1016/J.PNMRS.2019.11.002.

[110]   M. Casarin and V. M. Sglavo, "Influence of processing conditions on the microstructure of NiO-YSZ supporting anode for solid oxide fuel cells," *Ceram. Int.*, vol. 41, no. 2, pp. 2543–2557, Mar. 2015, doi: 10.1016/J.CERAMINT.2014.10.168.

[111]   W. H. Kan, A. J. Samson, and V. Thangadurai, "Trends in electrode development for next generation solid oxide fuel cells," *J. Mater. Chem. A*, vol. 4, no. 46, pp. 17913–17932, 2016.

[112]   M. Xin, L. Zhang, Y. Chang, L. Ren, X. Luo, and H. Zhou, "Modification of tape casting slurry via effective plasticization by butyl benzyl phthalate of CaO–SiO2–B2O3 glass–ceramics," *J.*

Mater. Sci. Mater. Electron., vol. 29, no. 24, pp. 20546–20553, Dec. 2018, doi: 10.1007/S10854-018-0207-6/FIGURES/11.

[113] R. K. Nishihora, P. L. Rachadel, M. G. N. Quadri, and D. Hotza, "Manufacturing porous ceramic materials by tape casting—A review," *J. Eur. Ceram. Soc.*, vol. 38, no. 4, pp. 988–1001, Apr. 2018, doi: 10.1016/J.JEURCERAMSOC.2017.11.047.

[114] V. M. Sglavo and M. Bertoldi, "Design and production of ceramic laminates with high mechanical resistance and reliability," *Acta Mater.*, vol. 54, no. 18, pp. 4929–4937, 2006, doi: 10.1016/j.actamat.2006.06.019.

[115] Z. Fu, A. Dellert, M. Lenhart, and A. Roosen, "Effect of pore orientation on anisotropic shrinkage in tape-cast products," *J. Eur. Ceram. Soc.*, vol. 34, no. 10, pp. 2483–2495, Sep. 2014, doi: 10.1016/J.JEURCERAMSOC.2014.03.002.

[116] A. Dellert, A. Heunisch, and A. Roosen, "The Origin of Anisotropic Shrinkage in Tape-Cast Green Tapes," *Int. J. Appl. Ceram. Technol.*, vol. 8, no. 6, pp. 1312–1319, Nov. 2011, doi: 10.1111/J.1744-7402.2011.02665.X.

[117] A. Heunisch, A. Dellert, and A. Roosen, "Effect of powder, binder and process parameters on anisotropic shrinkage in tape cast ceramic products," *J. Eur. Ceram. Soc.*, vol. 30, no. 16, pp. 3397–3406, Dec. 2010, doi: 10.1016/J.JEURCERAMSOC.2010.08.012.

[118] A. KARAS, T. KUMAGAI, and W. R. CANNON, "Casting behavior and tensile strength of cast BaTiO sub 3 tape," *Adv. Ceram. Mater.*, vol. 3:4, no. 4, pp. 374–377, Jul. 1988, doi: 10.1111/J.1551-2916.1988.TB00237.X.

[119] J. Li, D. Wang, Y. Shan, and H. Zhou, "Influence of binder content and the ratio of plasticizer to binder on tape casting and sintering performance of CaO–B2O3–SiO2–Al2O3 glass/Al2O3 ceramics," *J. Mater. Sci. Mater. Electron.*, vol. 31, no. 22, pp. 20022–20032, Nov. 2020, doi: 10.1007/S10854-020-04524-Y/FIGURES/12.

[120] Y. Duan, J. Zhang, X. Li, Y. Shi, J. Xie, and D. Jiang, "Optimization of the tape casting process for the development of high performance silicon nitride substrate," *Int. J. Appl. Ceram. Technol.*, vol. 14, no. 4, pp. 712–718, 2017, doi: 10.1111/ijac.12679.

[121]   M. Santaya, L. Toscani, L. Baqué, H. E. Troiani, and L. Mogni, "Study of phase stability of $SrTi_{0.3}Fe_{0.7}O_3−\delta$ perovskite in reducing atmosphere: Effect of microstructure," *Solid State Ionics*, vol. 342, p. 115064, Dec. 2019, doi: 10.1016/J.SSI.2019.115064.

[122]   E. Filonova and E. Pikalova, "Overview of Approaches to Increase the Electrochemical Activity of Conventional Perovskite Air Electrodes," *Materials (Basel).*, vol. 16, no. 14, 2023, doi: 10.3390/ma16144967.

[123]   P. Fedeli, F. Drago, F. Schulze-Küppers, and S. Baumann, "Asymmetric LSCF Membranes Utilizing Commercial Powders," *Materials (Basel).*, vol. 13, no. 3, p. 614, 2020.

[124]   F. Schulze-küppers, S. Baumann, F. Tietz, H. J. M. Bouwmeester, and W. A. Meulenberg, "oxygen transport membranes," *J. Eur. Ceram. Soc.*, vol. 34, no. 15, pp. 3741–3748, 2014, doi: 10.1016/j.jeurceramsoc.2014.06.012.

[125]   J. M. Serra, J. Garcia-Fayos, S. Baumann, F. Schulze-Küppers, and W. A. Meulenberg, "Oxygen permeation through tape-cast asymmetric all-$La_{0.6}Sr_{0.4}Co_{0.2}Fe_{0.8}O_3−\delta$ membranes," *J. Memb. Sci.*, vol. 447, pp. 297–305, Nov. 2013, doi: 10.1016/J.MEMSCI.2013.07.030.

[126]   L. Nie, Z. Liu, M. Liu, L. Yang, Y. Zhang, and M. Liu, "Enhanced Performance of $La_{0.6}Sr_{0.4}Co_{0.2}Fe_{0.8}O_3−\delta\delta$ (LSCF) Cathodes with Graded Microstructure Fabricated by Tape Casting," *J. Electrochem. Sci. Technol.*, vol. 1, no. 1, pp. 50–56, 2010.

[127]   Z. Liu, M. Liu, L. Nie, and M. Liu, "Fabrication and characterization of functionally-graded LSCF cathodes by tape casting," *Int. J. Hydrogen Energy*, vol. 38, no. 2, pp. 1082–1087, 2013, doi: https://doi.org/10.1016/j.ijhydene.2012.10.048.

[128]   H. Middleton, S. Diethelm, R. Ihringer, D. Larrain, J. Sfeir, and J. Van Herle, "Co-casting and co-sintering of porous MgO support plates with thin dense perovskite layers of $LaSrFeCoO_3$," *J. Eur. Ceram. Soc.*, vol. 24, no. 6, pp. 1083–1086, Jan. 2004, doi: 10.1016/S0955-2219(03)00554-5.

[129]   R. Fernández-González, T. Molina, S. Savvin, R. Moreno, A. Makradi, and P. Núñez, "Characterization and fabrication of LSCF tapes," *J. Eur. Ceram. Soc.*, vol. 34, no. 4, pp. 953–959, 2014, doi:

https://doi.org/10.1016/j.jeurceramsoc.2013.10.023.

[130] V. P. Junior, P. L. Rachadel, M. N. Quadri, D. Hotza, and S. Y. G. González, "Enhanced LSCF oxygen deficiency through hydrothermal synthesis," *Ceram. Int.*, vol. 44, no. 17, pp. 20671–20676, 2018, doi: 10.1016/j.ceramint.2018.08.060.

[131] E. Carlos, R. Martins, E. Fortunato, and R. Branquinho, "Solution Combustion Synthesis: Towards a Sustainable Approach for Metal Oxides," *Chemistry - A European Journal*, vol. 26, no. 42. Wiley-VCH Verlag, pp. 9099–9125, Jul. 27, 2020. doi: 10.1002/chem.202000678.

[132] Y. Jiang, S. Yang, Z. Hua, and H. Huang, "Sol-gel autocombustion synthesis of metals and metal alloys," *Angew. Chemie - Int. Ed.*, vol. 48, no. 45, pp. 8529–8531, 2009, doi: 10.1002/anie.200903444.

[133] S. Li, B. Bergman, and Z. Zhao, "Synthesis and characterization of lanthanum aluminate powders via a polymer complexing plus combustion route," *Mater. Chem. Phys.*, vol. 132, no. 2–3, pp. 309–315, Feb. 2012, doi: 10.1016/J.MATCHEMPHYS.2011.11.019.

[134] F. Deganello, "Nanomaterials for environmental and energy applications prepared by solution combustion based-methodologies: Role of the fuel," in *Materials Today: Proceedings*, Elsevier Ltd, Jan. 2017, pp. 5507–5516. doi: 10.1016/j.matpr.2017.06.006.

[135] F. Deganello and A. K. Tyagi, "Solution combustion synthesis, energy and environment: Best parameters for better materials," *Progress in Crystal Growth and Characterization of Materials*, vol. 64, no. 2. Elsevier Ltd, pp. 23–61, Jun. 01, 2018. doi: 10.1016/j.pcrysgrow.2018.03.001.

[136] S. K. Han and B. H. Jhun, "Effect of additives on the cloud point of polyethylene glycols," *Arch. Pharm. Res.*, vol. 7, no. 1, pp. 1–9, 1984, doi: 10.1007/BF02856915.

[137] R. Zurowski, M. Gluszek, A. Antosik, E. Pietrzak, G. Rokicki, and M. Szafran, "Copolymers dispersions designed to shaping of ceramic materials: Investigations of glass transition temperature, thermal stability and decomposition of water-thinnable binders," *J. Therm. Anal. Calorim.*, vol. 132, no. 1, pp. 453–461, Apr. 2018, doi: 10.1007/S10973-017-6955-3/FIGURES/6.

[138] X. Lu, J. R. G. Evans, and S. N. Heavens, "A comparison of the tape casting of α- and β-alumina," *J. Eur. Ceram. Soc.*, vol. 32, no. 16, pp. 4219–4228, Dec. 2012, doi: 10.1016/j.jeurceramsoc.2012.07.013.

[139] V. M. Sglavo, "Grand challenges in ceramics processing," *Front. Ceram.*, vol. 1, p. 1136720, Feb. 2023, doi: 10.3389/FCEIC.2023.1136720.

[140] Lv Houfu, "In situ Investigation of Reversible Exsolution/Dissolution of CoFe Nanoparticles in Perovskite," *STHE HITACHI Sci. Instrum. NEWS*, vol. 15, 2020.

[141] J. Laurencin *et al.*, "Degradation mechanism of La0.6Sr0.4Co0.2Fe0.8O3-δ/Gd0.1Ce0.9O2-δ composite electrode operated under solid oxide electrolysis and fuel cell conditions," *Electrochim. Acta*, vol. 241, pp. 459–476, 2017, doi: https://doi.org/10.1016/j.electacta.2017.05.011.

[142] D. Oh, D. Gostovic, and E. D. Wachsman, "Mechanism of La 0.6Sr 0.4Co 0.2Fe 0.8O 3 cathode degradation," *J. Mater. Res.*, vol. 27, no. 15, pp. 1992–1999, 2012, doi: 10.1557/jmr.2012.222.

[143] M. Lo Faro *et al.*, "Solid oxide fuel cells fed with dry ethanol: The effect of a perovskite protective anodic layer containing dispersed Ni-alloy @ FeOx core-shell nanoparticles," *Appl. Catal. B Environ.*, vol. 220, pp. 98–110, Jan. 2018, doi: 10.1016/J.APCATB.2017.08.010.

[144] N. Ni and S. Skinner, "Combined Cr and Mo poisoning of (La,Sr)(Co,Fe)O3−δ solid oxide fuel cell cathodes at the nanoscale," *Solid State Ionics*, vol. 288, pp. 28–31, 2016, doi: https://doi.org/10.1016/j.ssi.2015.12.030.

[145] B. C. Yang, J. Koo, J. W. Shin, D. Go, J. H. Shim, and J. An, "Direct Alcohol-Fueled Low-Temperature Solid Oxide Fuel Cells: A Review," *Energy Technol.*, vol. 7, no. 1, pp. 5–19, 2019, doi: 10.1002/ente.201700777.

[146] M. Cimenti, M. A. Buccheri, and J. M. Hill, "Direct Utilization of Methanol and Ethanol on La 0.75Sr 0.25Cr 0.5Mn 0.5O 3-δ Anodes for Solid Oxide Fuel Cells," *Electrocatalysis*, vol. 3, no. 1, pp. 59–67, 2012, doi: 10.1007/s12678-011-0076-8.

[147]   D. Han, Y. Liu, S. Wang, and Z. Zhan, "Electrochimica Acta temperature solid oxide fuel cell cathodes," *Electrochim. Acta*, vol. 143, pp. 168–174, 2014, [Online]. Available: http://dx.doi.org/10.1016/j.electacta.2014.07.153

[148]   G. Andrade, J. V₁, F. J. Mu, S. N, and F. Del Rio, "Advances in the development of titanates for anodes in SOFC ´ a Liliana Avalos," vol. 44, pp. 12529–12542, 2018.